The Astrophysical Journal, 834:193 (27pp), 2017 January 10 doi:10.3847/1538-4357/834/2/193

A HUNT FOR MASSIVE STARLESS CORES

Shuo Kong[1,2], Jonathan C. Tan[1,3], Paola Caselli[4], Francesco Fontani[5], Mengyao Liu[1], and Michael J. Butler[6]
[1] Dept. of Astronomy, University of Florida, Gainesville, FL 32611, USA
[2] Dept. of Astronomy, Yale University, New Haven, CT 06511, USA
[3] Dept. of Physics, University of Florida, Gainesville, FL 32611, USA
[4] Max-Planck-Institute for Extraterrestrial Physics (MPE), Giessenbachstr. 1, D-85748 Garching, Germany
[5] INAF—Osservatorio Astrofisico di Arcetri, L.go E. Fermi 5, I-50125, Florence, Italy
[6] Max Planck Institute for Astronomy, Königstuhl 17, D-69117 Heidelberg, Germany
Received 2016 September 19; revised 2016 November 28; accepted 2016 November 28; published 2017 January 13

ABSTRACT

We carry out an ALMA N_2D^+(3-2) and 1.3 mm continuum survey of 32 high-mass surface density regions of seven infrared dark clouds, with the aim of finding massive starless cores that may form the initial conditions for the formation of massive stars. Cores showing strong N_2D^+(3-2) emission are expected to be highly deuterated and indicative of early, potentially pre-stellar stages of star formation. We also present maps of these regions in ancillary line tracers, including $C^{18}O$(2-1), DCN(3-2), and DCO^+(3-2). Over 100 N_2D^+ cores are identified with our newly developed core-finding algorithm, based on connected structures in position–velocity space. The most massive core has $\sim$70 $M_\odot$ (potentially $\sim$170 $M_\odot$) and so may be representative of the initial conditions or early stages of massive star formation. The existence and dynamical properties of such cores constrain massive star formation theories. We measure the line widths and thus velocity dispersion of six of the cores with strongest N_2D^+(3-2) line emission, finding results that are generally consistent with virial equilibrium of pressure confined cores.

Key words: astrochemistry – ISM: clouds – ISM: kinematics and dynamics – ISM: magnetic fields – stars: formation – stars: massive

1. INTRODUCTION

Massive star formation remains an important unsolved problem in astrophysics. Here, we seek to obtain improved observational constraints on the initial conditions and early stages of the process. If there is a universal star formation mechanism, such that massive stars (>8 $M_\odot$) are born via a scaled-up version of the low-mass Core Accretion mechanism (e.g., McLaughlin & Pudritz 1997; McKee & Tan 2003, hereafter MT03), then the initial conditions (i.e., at the time just before protostar formation) should be massive starless cores. Here, the term "core" is defined to be the self-gravitating structure that will collapse to a single, central, rotationally supported disk that eventually forms a single star or small N multiple. Early stages of massive star formation by this mechanism would include a low-mass protostar undergoing relatively ordered accretion fed by quasi-monolithic collapse, near the center of a massive core. The existence of such cores is a key difference between this model and competitive accretion (e.g., Bonnell et al. 2001; Wang et al. 2010), which involves fragmentation of gas into protostellar seeds with initial masses only on the order of the thermal Jeans mass—typically much less than a solar mass in the high-mass surface density, high-pressure clumps where massive stars form. Note that the term "clump" is defined to mean the self-gravitating cloud that eventually fragments into a star cluster. Only later do some of these seeds accumulate further material, fed from the collapsing clump, to become massive stars. Thus, finding and characterizing massive starless and early-stage cores is a key way to distinguish between massive star formation theories.

However, because massive stars are rare, massive starless/early-stage cores—even if they exist, they would also be rare, and thus, typically distant and relatively small in angular size. Furthermore, they would likely be surrounded by much larger quantities of cold, dense molecular clump gas, with most mass going into lower mass stars or being dispersed back into the diffuse interstellar medium. Finding massive starless/early-stage cores is, thus, a challenging problem.

We have developed a strategy to overcome this challenge. We target regions based on mid-infrared extinction mapping of infrared dark clouds (IRDCs) (Butler & Tan 2009, 2012 hereafter BT09, BT12), which probes mass surface densities up to $\Sigma \sim 0.5$ g cm^{-2}, with an angular resolution of 2″. This allows detailed study of the structure of dense clumps: BT12 characterized 42 high Σ clumps selected from 10 IRDCs (A-J), which were chosen to be relatively nearby and dense. The 42 clumps were checked to make sure they are free of 8 and 24 μm (Spitzer-IRAC & MIPS) sources. We note that this method of sample selection differs from that based on following up strong mm continuum sources and then selecting those that are IR, including 70 μm, dark (e.g., Tackenberg et al. 2012; Traficante et al. 2015; Svoboda et al. 2016).

Our goal, which we carry out in this paper, is to search the majority of these sources for N_2D^+(3-2) line emission. The abundance of this species is known to increase in cold, dense conditions of low-mass starless cores (e.g., Crapsi et al. 2005; Bergin & Tafalla 2007; Caselli & Ceccarelli 2012), where CO is largely frozen-out onto dust grain ice mantles and thus depleted from the gas phase. The enhanced abundance of N_2D^+ with respect to N_2H^+ is relatively well-understood from the astrochemical point of view, and we have developed a comprehensive spin-state, gas phase reaction network to model this deuteration process (Kong et al. 2015, hereafter K15). It is this high abundance of N_2D^+ that acts as a signpost for the presence of a starless core on the verge of collapse, or an early-stage core just after protostar formation, allowing us to find these relatively rare locations in IRDCs.

We tested this method by observing four target regions centered on IRDC clumps with ALMA in Cycle 0, detecting 6 N_2D^+(3-2) cores at 2″ resolution ($\geqslant$1 from each region) (Tan et al. 2013, hereafter T13). The two most massive cores were found in the IRDC clump C1: C1-N and C1-S. We estimated the masses of the cores, defined by projection of their 3σ $l-b-v$ space N_2D^+(3-2) contour, in two ways: (1) from the MIREX map, finding C1-N has $61\pm30\,M_\odot$ and C1-S has $59\pm30\,M_\odot$ with the ~50% systematic uncertainty due to assumed distance (5 ± 1 kpc) and dust opacity (~30%) uncertainties; (2) from mm dust continuum emission, finding C1-N has $16_7^{33}\,M_\odot$ and C1-S has $63_{27}^{129}\,M_\odot$, with uncertainties mostly due to the adopted dust temperature of $T=10\pm3$ K, along with distance and dust emissivity uncertainties. Note that it is possible that, in general, the "core" may extend beyond the observed N_2D^+(3-2) contour, so these may be lower limits on the core mass. On the other hand, it is also possible that the N_2D^+(3-2) structure may actually contain more than one core, i.e., it may be resolved into two or more separate cores, if observed at higher angular resolution.

Thus, of the six T13 cores, C1-S and C1-N are the most promising examples of a massive starless/early-stage cores, i.e., with $\gtrsim$20 $M_\odot$ that may allow formation of a $\gtrsim$10 $M_\odot$ star, given expected outflow regulated formation efficiencies ~50% (Zhang et al. 2014). C1-S appears monolithic, centrally-concentrated in both N_2D^+(3-2) and mm continuum emission, and rounded (most likely by self-gravity). C1-N appears to be less centrally concentrated and potentially fragmented. Follow-up observations of other N_2D^+ and N_2H^+ lines allowed measurement of $D_{\rm frac}\equiv[N_2D^+]/[N_2H^+]$ in the cores, with values of 0.2–0.7 (Kong et al. 2016). For most chemodynamical models, such high values (orders of magnitude greater than the cosmic [D]/[H] ratio of $\sim10^{-5}$) imply relatively old astrochemical ages, and thus, relatively slow collapse rates, $\lesssim1/3$ of the rate of free-fall collapse.

Further follow-up with ALMA in Cycle 2 of the C1 region found the presence of a very collimated protostellar outflow, traced by ^{12}CO(2-1), from a source within C1-S (in both position and velocity space), such that this is most likely to be an example of an early-stage massive core (Tan et al. 2016). A second protostellar outflow source also overlaps spatially with C1-S, although its association with the core in velocity space is less certain. No outflows were seen from C1-N.

T13 used the N_2D^+(3-2) line-width to study the dynamics of the cores. For the sample of six sources, the velocity dispersions were, on average, consistent (within a factor of ~0.8) with those expected from virial equilibrium of the fiducial MT03 Turbulent Core model. However, for C1-S, the observed velocity dispersion is about a factor of two smaller than the fiducial virial equilibrium prediction. If virial equilibrium is being maintained, as would be expected if the astrochemical age is larger than the dynamical time, then relatively strong magnetic fields, ~1 mG, are needed.

We see that larger samples of starless and early-stage cores are needed to better test the different theoretical models. This has motivated the observations and analysis presented in this paper.

2. SAMPLE SELECTION AND ALMA OBSERVATIONS

BT09 and BT12 studied the 10 IRDCs A-J, selecting them from the sample of Rathborne et al. (2006) to be particularly suitable for MIREX mapping: they are relatively nearby (thus reducing the contribution of MIR foreground emission), show high contrast against the Galactic MIR background, and are surrounded by relatively simple, smooth MIR background emission. BT12 analyzed the detailed structural properties of 42 clumps selected from these clouds to be dark at 8 and 24 μm, the latter evaluated from the MIPSGAL survey (Carey et al. 2009). T13 observed N_2D^+(3-2) in 4 clumps, C1, F1, F2, G2, with ALMA in Cycle 0.

With ALMA in Cycle 2 (Project number: 2013.1.00806.S; PI: Tan), we observed 32 more clumps from the BT12 sample (listed in Table 1), focusing on IRDCs A, B, C, D, E, F, and H. The observations were carried out during 2015 April, with the 12 m array in the most compact configuration. The baselines were from 12 to 330 m (9–254 kλ), resulting in a synthesized beam size of $1\farcs5\times1\farcs0$ and a maximum detectable scale of ~20″. The diameter of the primary beam, which approximately sets the field-of-view (FOV), is ~26″. The maximum scale is comparable to the FOV, and ALMA has very good uv-coverage in the short spacings in the compact configuration. No ACA observations were performed. Two of the target pointings contained two BT12 clumps; in total, there were 30 pointings in our observations (two tracks, each of 15 pointings). Together with the four targets already observed, this completes 86% of the BT12 sample (92% of the sources in IRDCs A-H, which are at a range Galactic longitudes from $l=18\fdg8$ to $35\fdg5$).

Dual polarization mode was adopted for the Band 6 spectral setup. Four basebands and seven spectral windows were used during the observations. A Baseband 1 single spectral window was centered on N_2D^+(3-2) (rest frequency 231.32 GHz), with a velocity resolution of 0.05 km s^{-1}. A Baseband 2 single spectral window was used for a continuum observation, centered at 231.00 GHz. The total bandwidth for this baseband is about 2 GHz. A Baseband 3 single spectral window was centered on C^{18}O(2-1) (rest frequency 219.56 GHz), with a velocity resolution of 0.05 km s^{-1}. Baseband 4 was split into four spectral windows, including a window at 216.11 GHz for DCO^+(3-2), a window at 216.95 GHz for CH_3OH($v\,t=0$ 5(1, 4)-4(2, 2), with upper-state energy of 56 K), a window at 217.10 GHz for SiO(5-4), and a window at 217.24 GHz for DCN(3-2). Each of these lines has a 0.2 km s^{-1} velocity resolution.

This paper will focus mostly on the results from the continuum and N_2D^+(3-2) observations, although the integrated intensity maps of most of the other species are also presented. The SiO(5-4) data, which probe protostellar outflows, are presented by M. Liu et al. (2016, in preparation).

The sample of 30 targets was divided into two tracks, each containing 15 sources. Track 1, with reference velocity of +58 km s^{-1}, includes A1, A2, A3, ($v_{\rm LSR}\simeq+66$ km s^{-1}: these estimates are derived from ^{13}CO(1-0) emission from the clouds: see, e.g., Hernandez & Tan 2015), B1, B2 ($v_{\rm LSR}\simeq+26$ km s^{-1}), C2,[7] C3, C4, C5, C6, C7, C8, C9 ($v_{\rm LSR}\simeq+79$ km s^{-1}), E1, and E2 ($v_{\rm LSR}\simeq+80$ km s^{-1}). Track 2, with reference velocity of +66 km s^{-1}, includes D1, D2 (also contains D4), D3, D5 (also contains D7), D6, D8, D9 ($v_{\rm LSR}\simeq+87$ km s^{-1}), F3, F4 ($v_{\rm LSR}\simeq+58$ km s^{-1}), H1, H2, H3, H4, H5, and H6[8] ($v_{\rm LSR}\simeq+44$ km s^{-1}). In Track 1,

[7] We note that the C2 region was studied by Zhang et al. (2015), including an observation of N_2D^+ with a sensitivity of 0.0075 Jy bm^{-1} per 0.7 km s^{-1}. They detected several mm continuum cores in this region, most of which appear to be protostellar.

[8] Also studied by Henshaw et al. (2016) with ALMA Band 7 observations, detecting multiple sub-mm continuum cores, including some embedded in very narrow filamentary structures.

Table 1
IRDC Clump Targets of the ALMA Cycle 2 Observation

Clump[a]	R.A.	Decl.	l (deg)	b (deg)	v_{LSR} (km s^{-1})	d (kpc)
A1	$18^h26^m15^s.14$	$-12°41'43''.4$	18.78675	−0.28592	66	4.8
A2	$18^h26^m19^s.04$	$-12°41'14''.8$	18.80117	−0.29625	66	4.8
A3	$18^h26^m21^s.78$	$-12°41'10''.2$	18.80750	−0.30550	66	4.8
B1	$18^h25^m52^s.83$	$-12°04'52''.7$	19.28758	0.08083	26	2.4
B2	$18^h25^m58^s.29$	$-12°04'13''.5$	19.30758	0.06625	26	2.4
C2	$18^h42^m50^s.45$	$-04°03'17''.7$	28.34383	0.06017	79	5.0
C3	$18^h42^m44^s.02$	$-04°01'54''.5$	28.35217	0.09450	79	5.0
C4	$18^h42^m49^s.34$	$-04°02'27''.3$	28.35417	0.07067	79	5.0
C5	$18^h42^m52^s.59$	$-04°02'44''.3$	28.35617	0.05650	79	5.0
C6	$18^h42^m54^s.37$	$-04°02'31''.7$	28.36267	0.05150	79	5.0
C7	$18^h42^m40^s.01$	$-04°00'34''.4$	28.36433	0.11950	79	5.0
C8	$18^h42^m59^s.99$	$-04°01'33''.1$	28.38783	0.03817	79	5.0
C9	$18^h42^m51^s.86$	$-03°59'43''.3$	28.39950	0.08217	79	5.0
D1	$18^h44^m17^s.05$	$-04°02'01''.5$	28.52717	−0.25033	87	5.7
D2	$18^h44^m23^s.79$	$-04°02'11''.5$	28.53750	−0.27650	87	5.7
D3	$18^h44^m15^s.38$	$-04°00'50''.7$	28.54150	−0.23517	87	5.7
D4	$18^h44^m22^s.51$	$-04°01'53''.5$	28.53950	−0.26950	87	5.7
D5	$18^h44^m16^s.43$	$-03°59'22''.3$	28.56533	−0.22783	87	5.7
D6	$18^h44^m17^s.78$	$-04°00'12''.4$	28.55550	−0.23917	87	5.7
D7	$18^h44^m17^s.69$	$-03°59'26''.5$	28.56667	−0.23300	87	5.7
D8	$18^h44^m18^s.29$	$-03°59'06''.2$	28.57283	−0.23267	87	5.7
D9	$18^h44^m18^s.74$	$-03°58'13''.7$	28.58667	−0.22767	87	5.7
E1	$18^h43^m06^s.71$	$-03°45'09''.9$	28.64350	0.13817	80	5.1
E2	$18^h43^m10^s.12$	$-03°45'15''.8$	28.64850	0.12483	80	5.1
F3	$18^h53^m18^s.42$	$+01°27'33''.9$	34.44383	0.24967	58	3.7
F4	$18^h53^m18^s.51$	$+01°28'30''.5$	34.45800	0.25650	58	3.7
H1	$18^h57^m11^s.37$	$+02°07'27''.1$	35.47800	−0.31033	44	2.9
H2	$18^h57^m06^s.92$	$+02°08'20''.9$	35.48283	−0.28700	44	2.9
H3	$18^h57^m08^s.83$	$+02°08'24''.3$	35.48733	−0.29367	44	2.9
H4	$18^h57^m06^s.88$	$+02°08'44''.8$	35.48867	−0.28383	44	2.9
H5	$18^h57^m08^s.27$	$+02°08'57''.7$	35.49450	−0.28733	44	2.9
H6	$18^h57^m08^s.17$	$+02°10'51''.8$	35.52250	−0.27250	44	2.9

Note.
[a] Targets selected from BT12.

J1924-2914 was used as the bandpass calibrator, J1832-1035 was used as the gain calibrator, and Neptune was the flux calibrator. In Track 2, J1751+0939 was used as the bandpass calibrator, J1851+0035 was used as the gain calibrator, and Titan was the flux calibrator. The continuum data were cleaned, but the line data were not cleaned due to their relatively weak detections. No self-calibration was done to the data set. Primary beam correction was applied before fluxes were extracted.

Our sensitivity level was determined by the desire to detect massive N_2D^+ cores that are similar to C1-S with $\gtrsim 5\sigma$ significance integrating over the typical velocity range of such cores, $\sim$1 km s^{-1}. We estimated this to be a sensitivity level of 30 mJy per beam per 0.1 km s^{-1}, i.e., three times worse than that achieved by T13. In the end, Track 1 has a sensitivity of 22 mJy beam^{-1} per 0.1 km s^{-1}. In Track 2, the sensitivity was 30 mJy beam^{-1} per 0.1 km s^{-1}. A 5 km s^{-1} integration results in a noise level of 21 mJy beam^{-1} km s^{-1}. The continuum sensitivity we achieve now is 0.22 mJy beam^{-1}, compared with T13's value of 0.27 mJy per $2''.3 \times 2''.0$ beam.

3. CORE DETECTION ANALYSIS METHODS

Our main goal is to systematically identify N_2D^+(3-2) cores, eventually presenting a rank ordering of cores via their N_2D^+ line flux, which extends down to relatively weak cores—for which there begins to be possible confusion with noise fluctuations. We will utilize the information of collocation of the cores with other tracers (e.g., 1.3 mm continuum emission and other line tracers) to help assess the reliability of the N_2D^+(3-2) cores. For the strongest cores, we will then estimate masses from both 1.3 mm dust emission and from the MIREX maps. Those cores with $\gtrsim 10\ M_\odot$ and without star-forming activity are good candidates to be massive starless cores.

We start by identifying cores as connected groups of "voxels" (pixels in 3D position–position–velocity (PPV) space of $l - b - v$) with flux densities of $\geqslant 3\sigma$ ("first threshold"), where σ is the noise level in each voxel. Note that this search is done in the cube before primary beam correction, to avoid spurious features at the edge of the maps; also, we restrict the core finding to within a field of view defined by the primary beam diameter. However, the noise level, σ, depends on the velocity resolution to which we smooth the data. After some experimentation (discussed below), we settle on a choice of a velocity resolution of 0.15 km s^{-1} (i.e., three times coarser than the full resolution of the data cubes), which has $\sigma \simeq 0.020$ Jy bm^{-1} for IRDCs A, B, C, and E, (Track 1) and $\sigma \simeq 0.030$ Jy bm^{-1} for IRDCs D, F, and H (Track 2). Next, searching only within the FOV of diameter of $26''$ (i.e., the half-power response diameter of the primary beam, i.e., where the sensitivity is reduced by about 50%), we identify all voxels above the 3σ threshold.

The selected voxels are then denoted as "nodes" (as in Graph theory). If two nodes are connected, i.e., adjacent in $l - b - v$ space, they are connected with an "edge." Once the data cube is traversed, we have a set of nodes and edges—and thus, a graph. Note that the graph so constructed has no directional information (i.e., an "undirected graph"): if voxel A is connected to voxel B, so is voxel B to voxel A. Next, using the NetworkX package (Hagberg et al. 2008), we identify all connected components in the graph, each of them being a core candidate.

After checking the results and comparing with the region (clump-scale) integrated intensity maps of N_2D^+(3-2) (using a 5 km s^{-1} velocity range), we notice some potential N_2D^+(3-2) structures that are not found by the above selection method. These structures have very few voxels that are above the first core threshold. However, they show continuous positive flux in velocity space. This leads us to amend our voxel selection: for already identified $\geqslant 3\sigma$ voxels, we consider their neighboring voxels and count them as part of the core, i.e., as nodes in the Graph, if they have a positive N_2D^+(3-2) line flux. The effect of this is to add the contribution of a halo of N_2D^+(3-2) line emission around the stronger peaks.

One can see that core selection may depend on a number of choices of criteria, including PPV cube velocity resolution, noise selection thresholds, and minimum angular size. We considered a variety of velocity resolutions with which to smooth the data cubes, which have an original full resolution of 0.05 km s^{-1}. Based on the observations of T13, N_2D^+(3-2) cores show line widths (including hyperfine broadening) as narrow as $\sim$0.5 km s^{-1}. Therefore, although we have adopted a smoothing of the data to 0.15 km s^{-1} resolution, we also make it a requirement that the core is detected in at least two adjacent channels. Because the ALMA data, by default, is Hanning smoothed, two neighboring channels are potentially correlated. Thus, a noise spike could potentially span across two channels, even when smoothed to 0.15 km s^{-1}, causing a false detection. To eliminate such false cores, we re-make the PPV cube with a 0.075 km s^{-1} velocity shift in the boundaries of the velocity channels, and require cores to also be identified in this cube. The 0.075 km s^{-1} shift is more than twice the finest channel spacing of the raw data, so these two cubes provide a good cross check to rule out noise spike features. Finally, we impose a condition of a minimum number of voxels that span an area on the sky that is comparable to the synthesized beam. This condition also helps mitigate false detections due to noise spikes.

Once N_2D^+(3-2) cores have been identified, we make additional checks of other tracers co-located at the core position and velocity. At the position of an N_2D^+ core, we check the signal in the continuum image and the 0th-moment images of DCO^+(3-2) and $C^{18}O$(2-1). Based on the observational results from T13, all N_2D^+ cores have corresponding DCO^+ and continuum emission. In cold starless cores, CO and its isotopologues should suffer heavy depletion via freeze-out on to dust grains, thus significantly reducing the flux in, e.g., $C^{18}O$(2-1). However, note that these checks are not used in core selection, but only to provide additional information that can then be used to assess the reality of the N_2D^+ core.

Finally, having obtained our sample of selected N_2D^+(3-2) cores, we re-examine their correspondence in the region (clump-scale) integrated intensity maps of N_2D^+(3-2) that use a 5 km s^{-1} velocity range (thus, with a higher noise level). The strongest cores are easily visible in this map, but many of the weaker ones do not stand out above the noise. In addition, there remain some $\geqslant 4\sigma$ features visible in the region maps that have not been identified as cores by our above method (i.e., as connected structures in PPV space). Because our focus is on the cores, we simply note the position of these "clump-scale" structures and carry out simple checks with other tracers to gauge their reality.

Our adopted method of finding cores, like any method, does involve some somewhat arbitrary choices for core definition and extraction. Thus, we have compared it to the "clumpfind" method in the yt package (Smith et al. 2009). We carried out the comparison in the B1 region. If we set the minimum size as the synthesized beam size, the search radius as the primary beam, and the threshold as 2.5σ, then yt finds all B1 cores given by our method. We consider that both methods find the coherent signals in the PPV cube. Ultimately, though, the precise definition used for a core will influence the final results. Thus, when comparing, for example, to the outputs of numerical simulations, similar analysis methods should be adopted where possible.

4. RESULTS

4.1. Overview of the 32 IRDC Clumps

Figures 1 through 10 present summary maps of the 30 targets, with one column for each source. Note that, except in the cases of D2 and D5, the FOV is centered on the IRDC core/clump Σ peak from BT12. The D2 region includes both D2 and (part of) D4, whereas the D5 region includes both D5 and D7. In these cases, the FOV is centered in between the Σ peaks. In all panels, the colored background shows MIREX-estimated mass surface density, Σ, in g cm^{-2}, from BT12. All panels also show the primary beam diameter FOV, which delimits the region that is searched for N_2D^+(3-2) cores. The locations ("+" signs) and names (XXA, XXB, XXC..., indicating the ordering of decreasing N_2D^+(3-2) line flux) of these cores are also shown. These cores are discussed below, in Section 4.2. The panels also indicate the locations ("×" signs) of N_2D^+(3-2) "clump-scale" structures with $\geqslant 4\sigma$ peaks in the 5 km s^{-1} velocity range 0th-moment map that are not found by our N_2D^+(3-2) core detection algorithm.

In the top row, the contours show 1.3 mm continuum emission. All regions generally have very strong continuum detection (C3 only has a 3σ detection, while D2 has 4σ detection). There is often quite good correspondence between the 1.3 mm continuum structures and those seen in the BT12 MIREX maps. Note, however, that the mm continuum image is insensitive to the structures that are larger than the maximum recoverable scale of the observation (i.e., $\gtrsim 20''$), unlike the MIREX map. Still, there are many regions where a MIREX Σ peak is not an especially strong mm continuum source and vice versa. Such discrepancies may arise because of problems in the MIREX map (e.g., where MIR bright sources are present) and/or if the mm continuum emission is being enhanced by higher temperatures, e.g., from local protostellar heating. A lack of prominent mm continuum emission from high Σ MIREX peaks may indicate these regions are extremely cold.

In the second row, the contours show N_2D^+(3-2) integrated intensity (0th-moment map). Here, and for all 0th-moment maps, the integration spans a velocity range of 5 km s^{-1} centered on

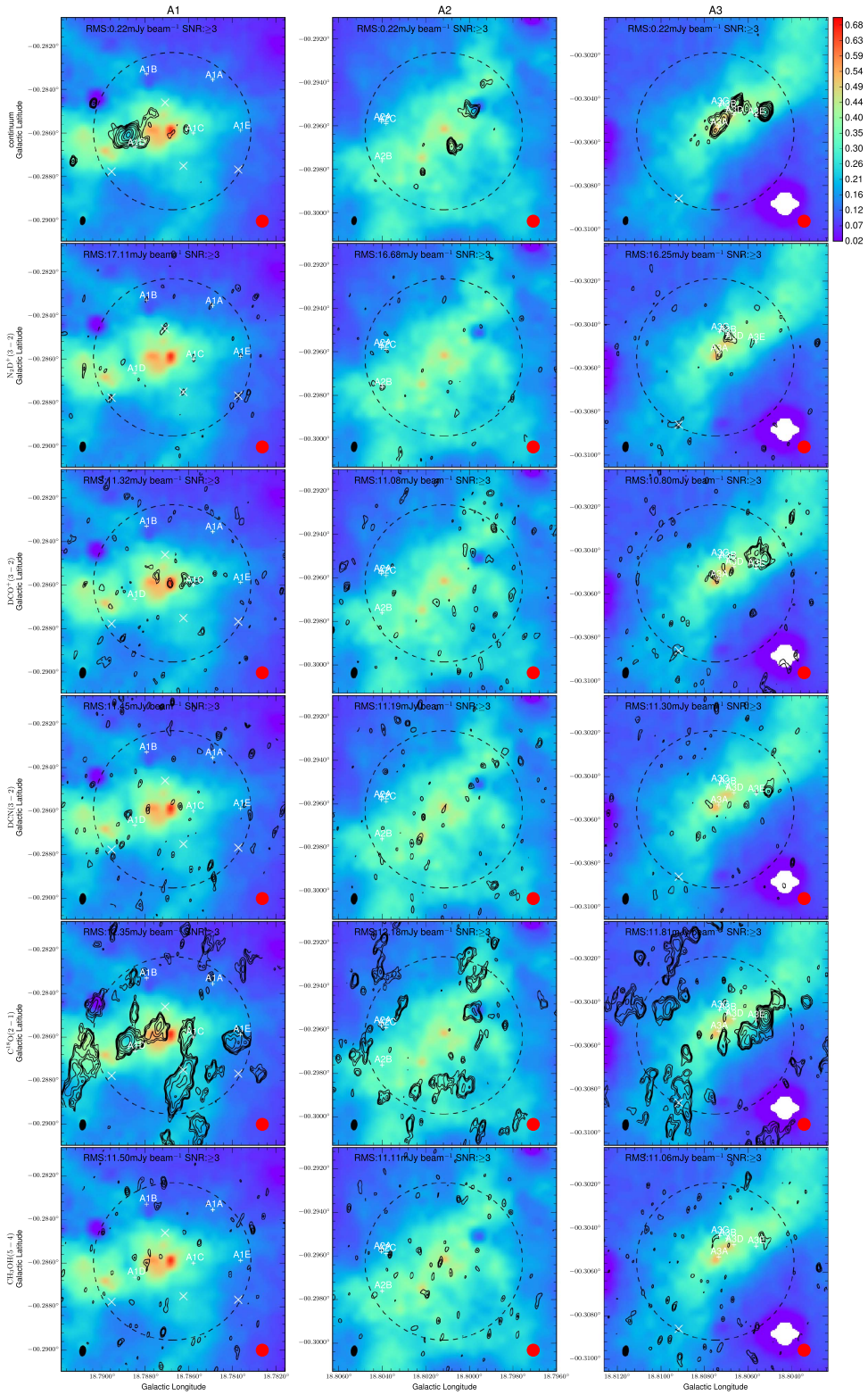

Figure 1. Summary figures for the surveyed IRDC clumps. Columns from left to right show the results for sources A1, A2, A3 (other sources continue in subsequent figures). The color-scale background shows MIREX mass surface density map from BT12. The color bar at the top-right corner indicates the scale in g cm^{-2}, which is preserved throughout all 30 columns. The white regions are locations of MIR bright sources, where the map is undefined. The ALMA survey results are shown as contours. From top to bottom, the contours show 1.30 mm continuum, integrated intensities of N_2D^+(3-2), DCO^+(3-2), DCN(3-2), $C^{18}O$(2-1), CH_3OH($v\,t = 0$ 5(1,4)-4(2,2)). The contour levels are in unit of σ, starting from 3σ, 4σ, 5σ, 7σ, 10σ, 15σ, 20σ, 30σ, 40σ, 50σ, 70σ, 100σ, 130σ, 160σ, 190σ... The σ for 1.30 mm continuum is 2.2×10^{-4} Jy bm^{-1}. The integrated intensity maps are made within a 5 km s^{-1} velocity range, with a σ of about 0.02 Jy bm^{-1} km s^{-1}. In each panel, the diameter of the primary beam is shown with the dashed circle and the *ALMA* beam on the lower left, and *Spitzer* 8 μm beam on the lower right (which sets the resolution of the MIREX map). Each panel also shows locations of N_2D^+(3-2) cores identified as connected structures in PPV space with "+" signs, along with the core names, e.g., A1A. Note that sometimes these cores do not appear as $\geqslant 3\sigma$ features in the integrated intensity map of N_2D^+(3-2) in the second row (see text). Sometimes $\geqslant 4\sigma$ features that are seen in this map are not associated with identified cores, and these are marked with "×" signs (see text).

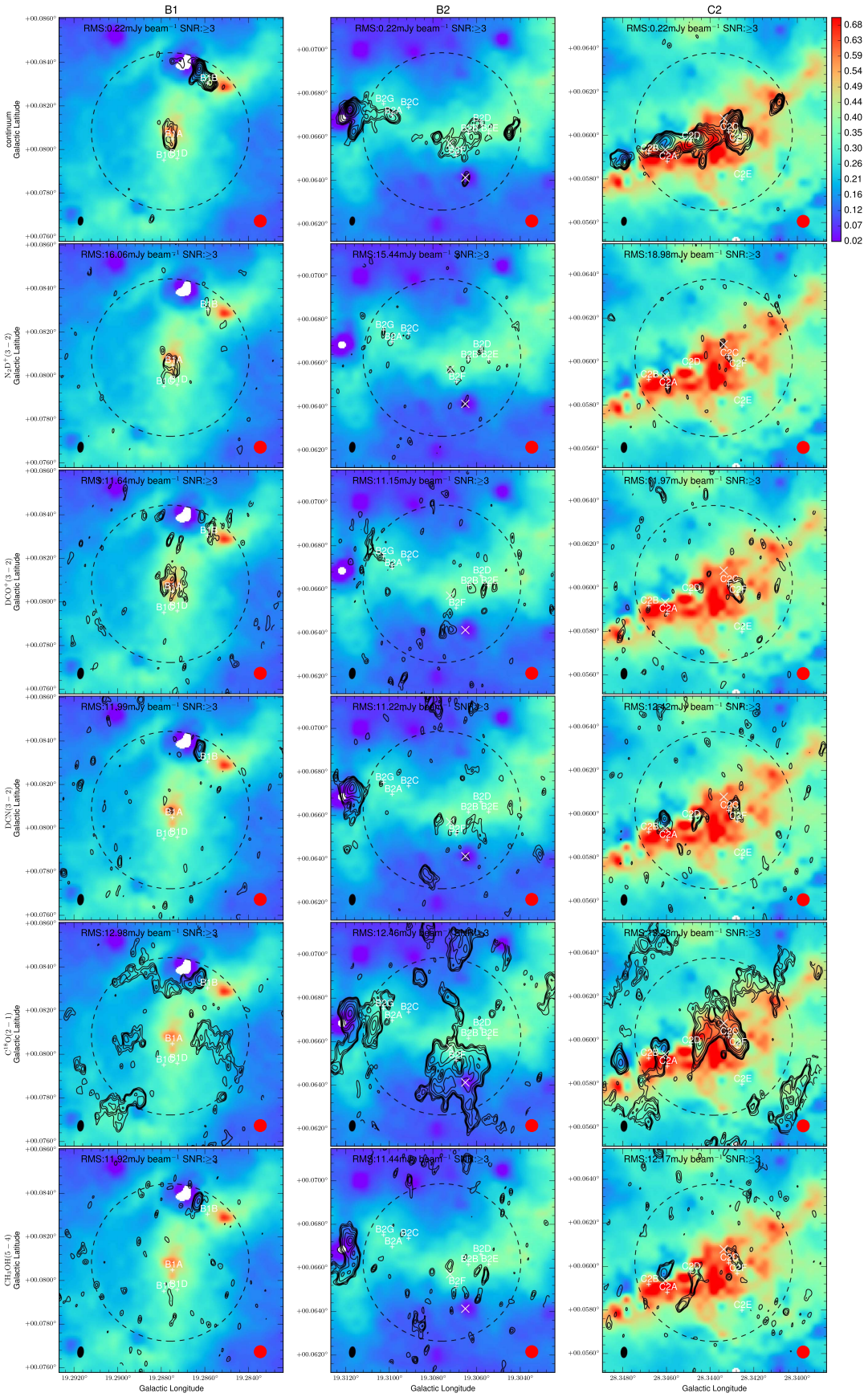

Figure 2. Same as Figure 1, but for sources B1, B2, and C2.

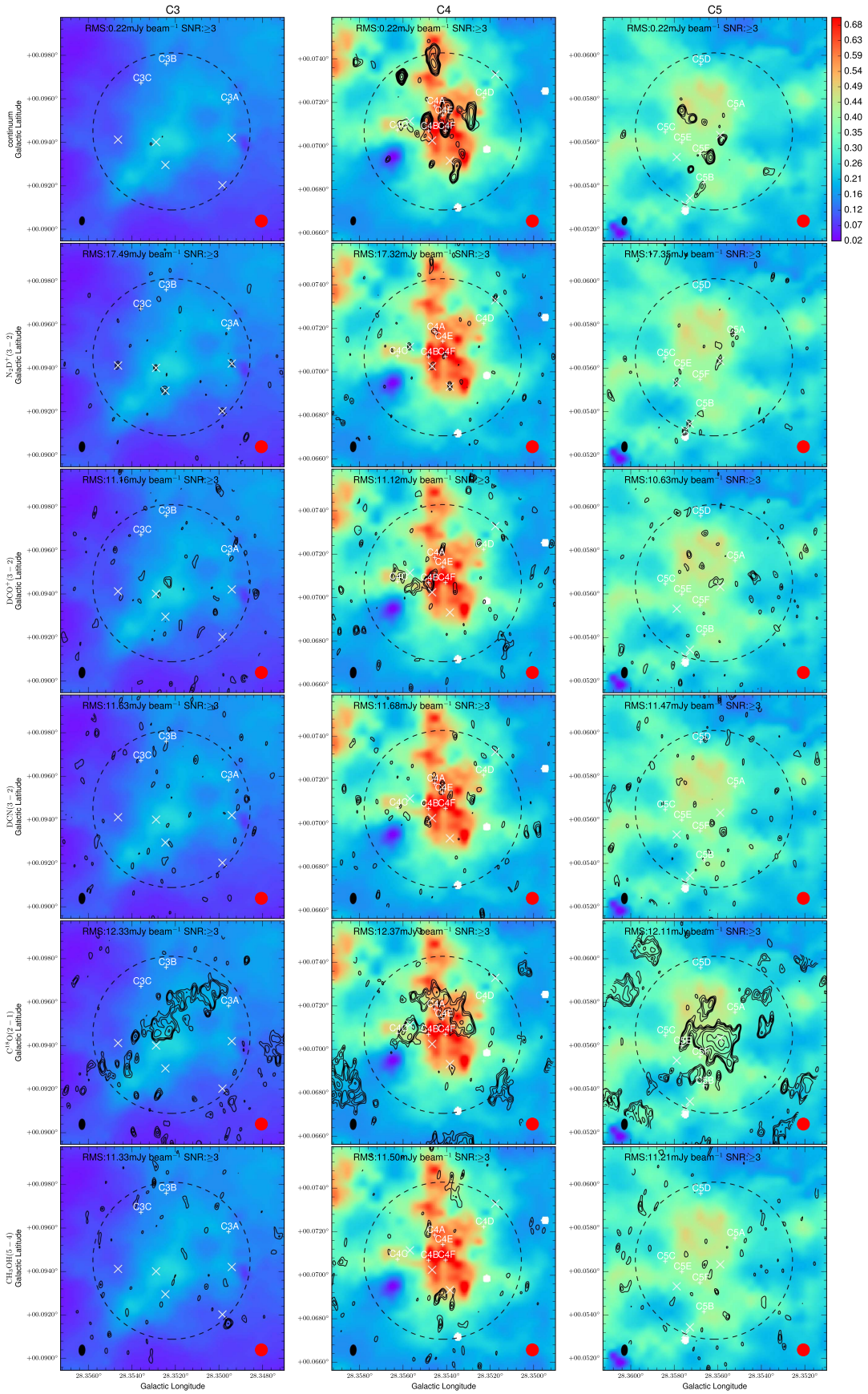

Figure 3. Same as Figure 1, but for sources C3, C4, and C5.

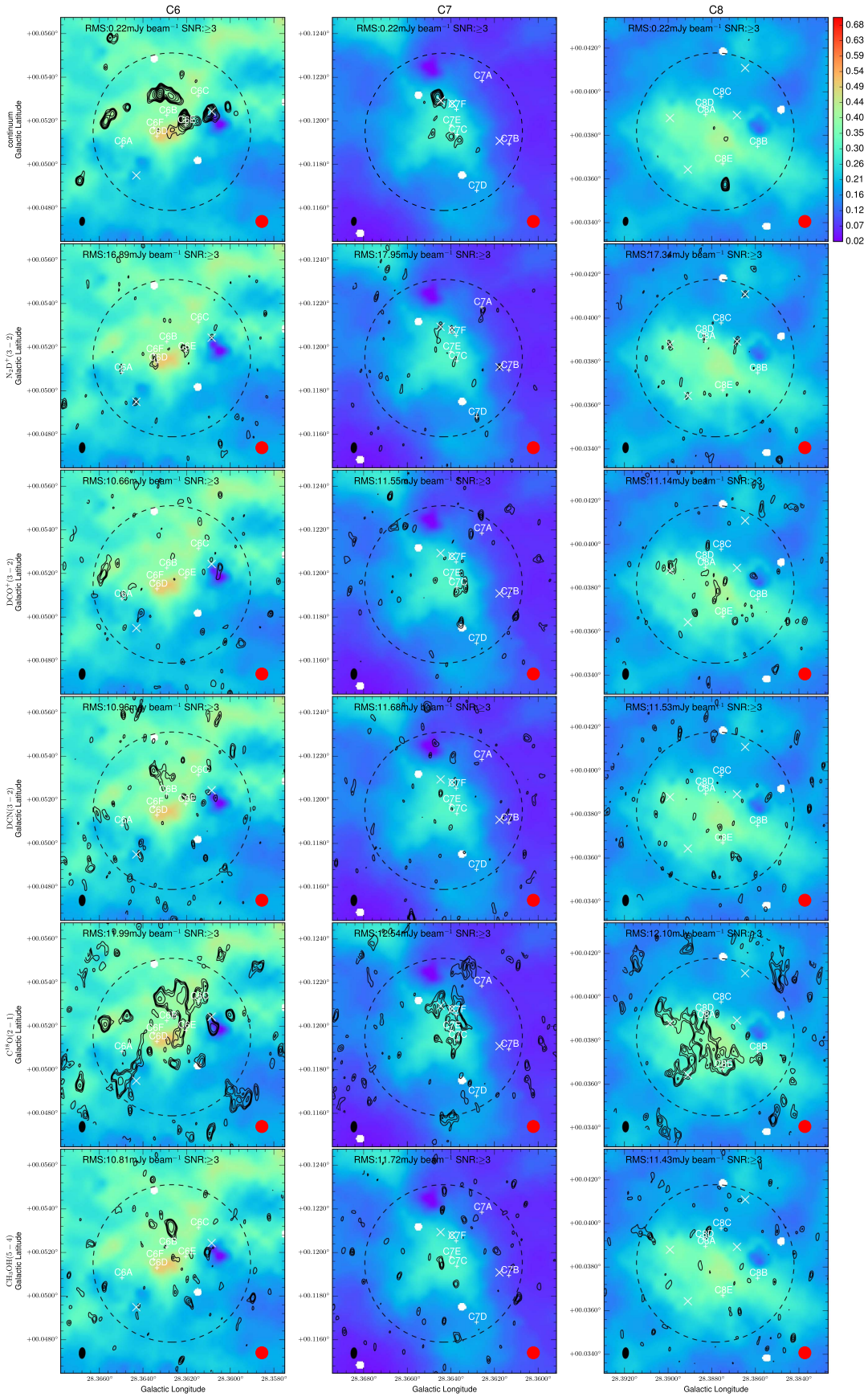

Figure 4. Same as Figure 1, but for sources C6, C7, and C8.

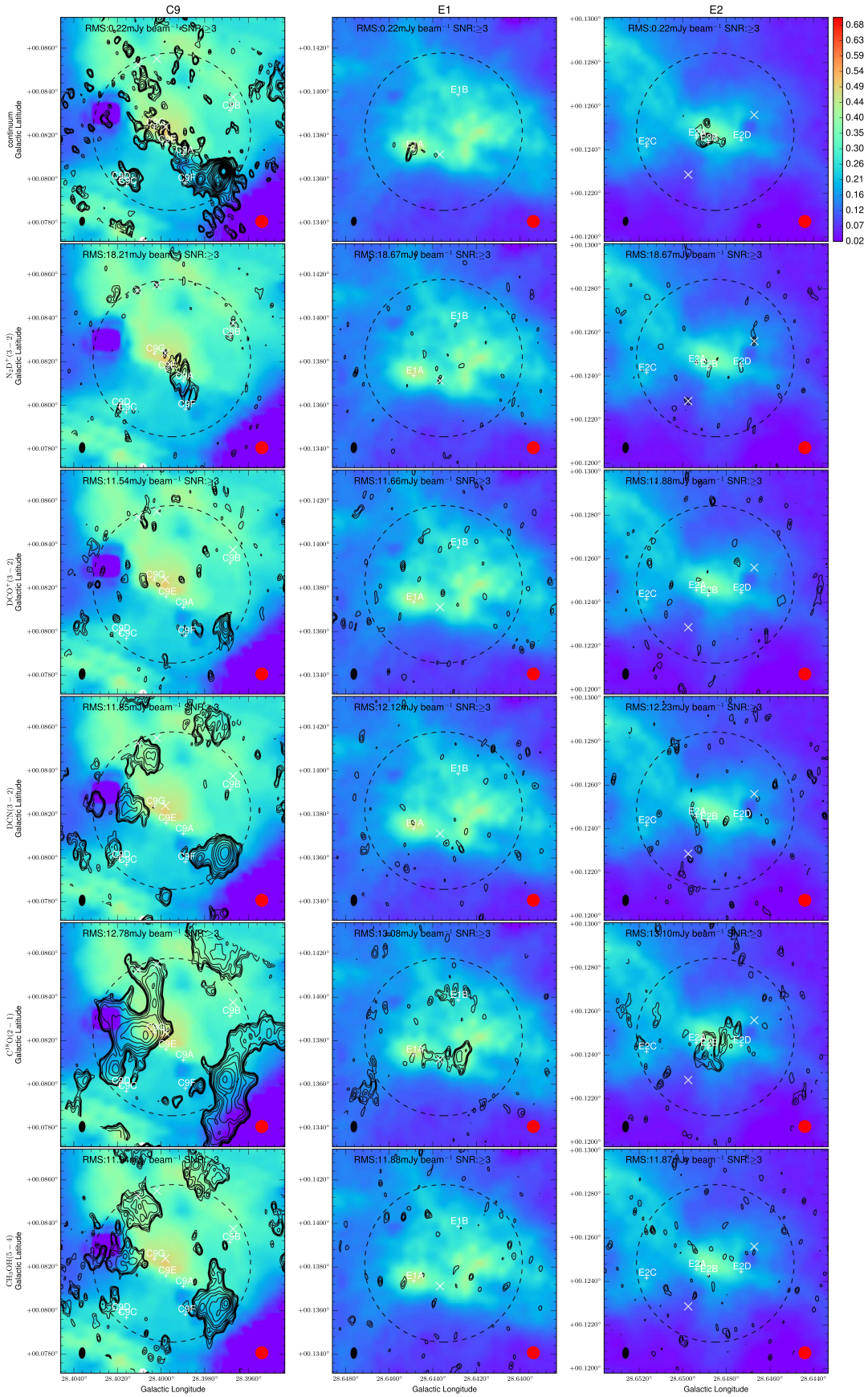

Figure 5. Same as Figure 1, but for sources C9, E1, and E2.

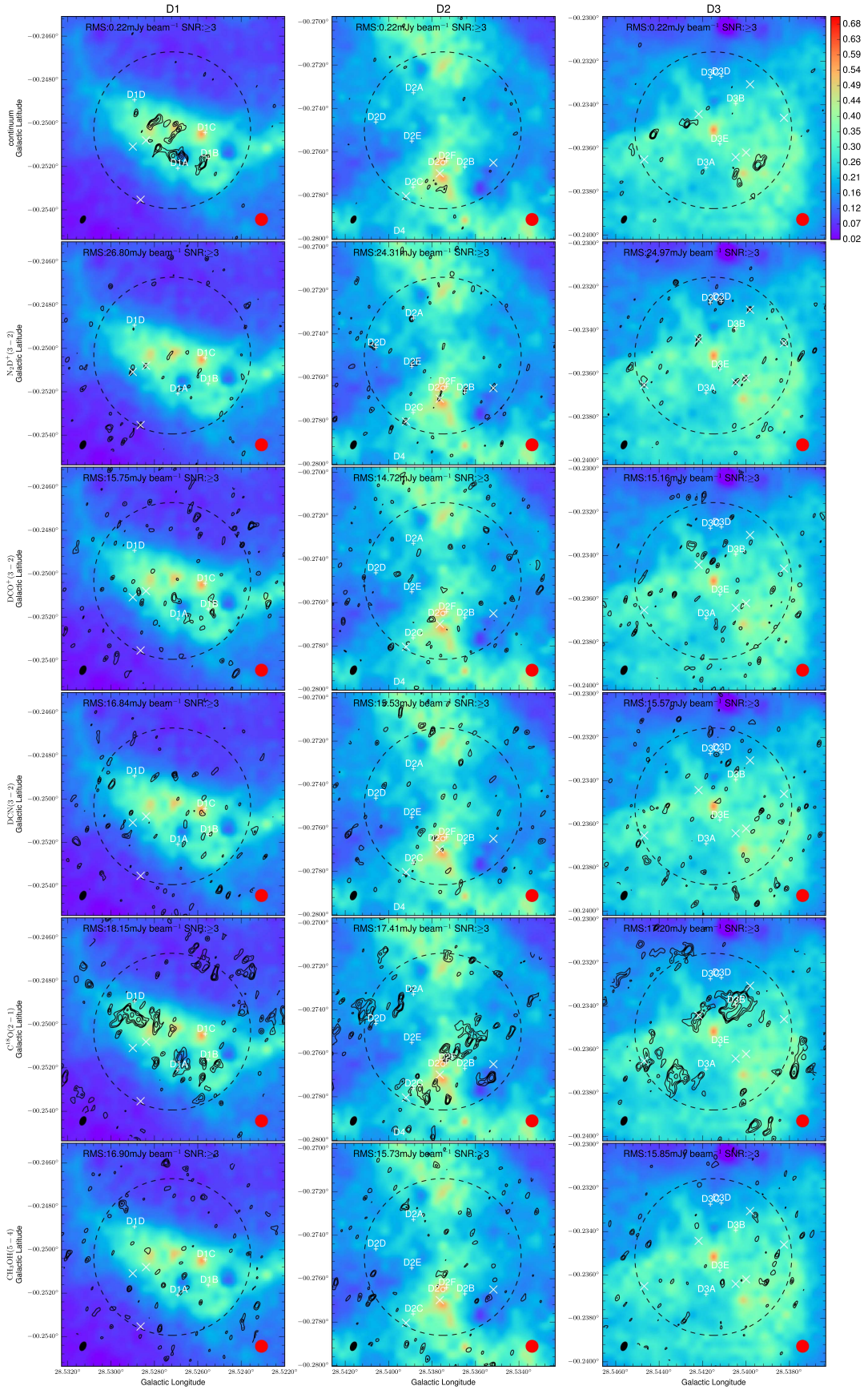

Figure 6. Same as Figure 1, but for sources D1, D2, and D3. Note that the center of the D2 core/clump from BT12 is shown with an open circle. The D4 complex is at the top of the D2 box (i.e., only partially within the 26″ diameter primary beam FOV), and the center of the D4 core/clump from BT12 is just outside the displayed box. For naming purposes, we assign all identified cores to D2.

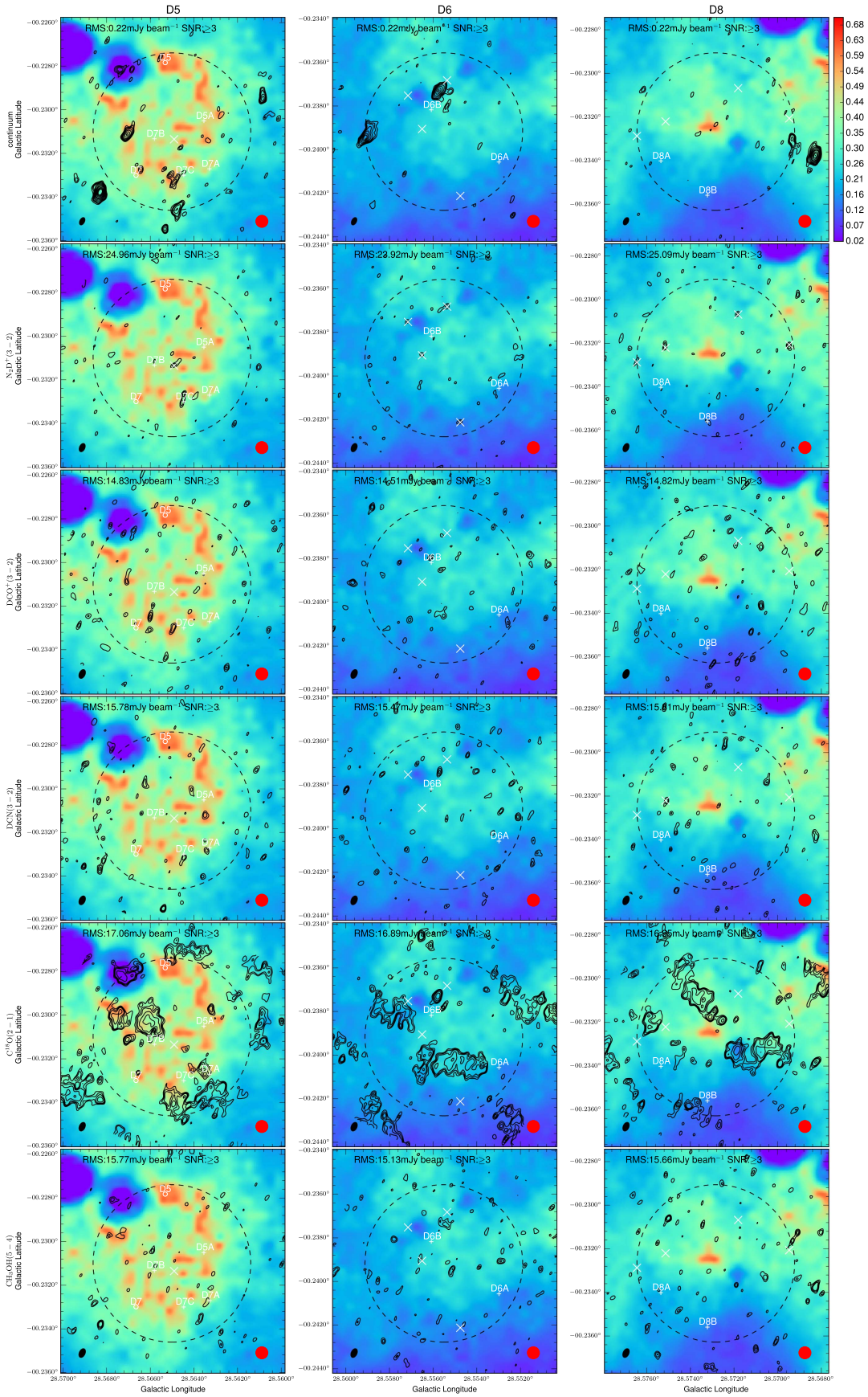

Figure 7. Same as Figure 1, but for sources D5, D6, and D8. Note that the D5 box also contains D7, and the centers of these core/clumps from BT12 are shown with open circles.

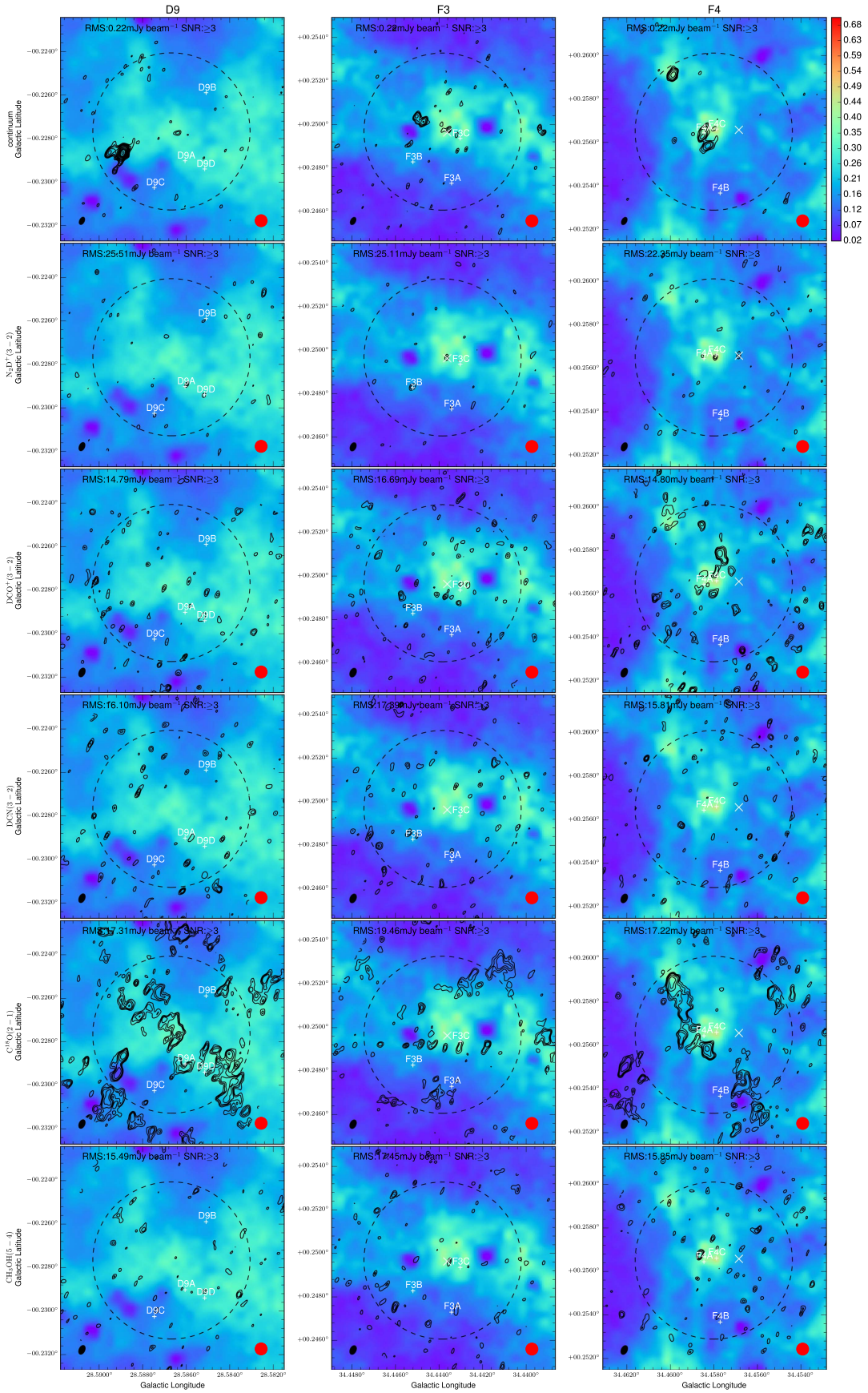

Figure 8. Same as Figure 1, but for sources D9, F3, and F4.

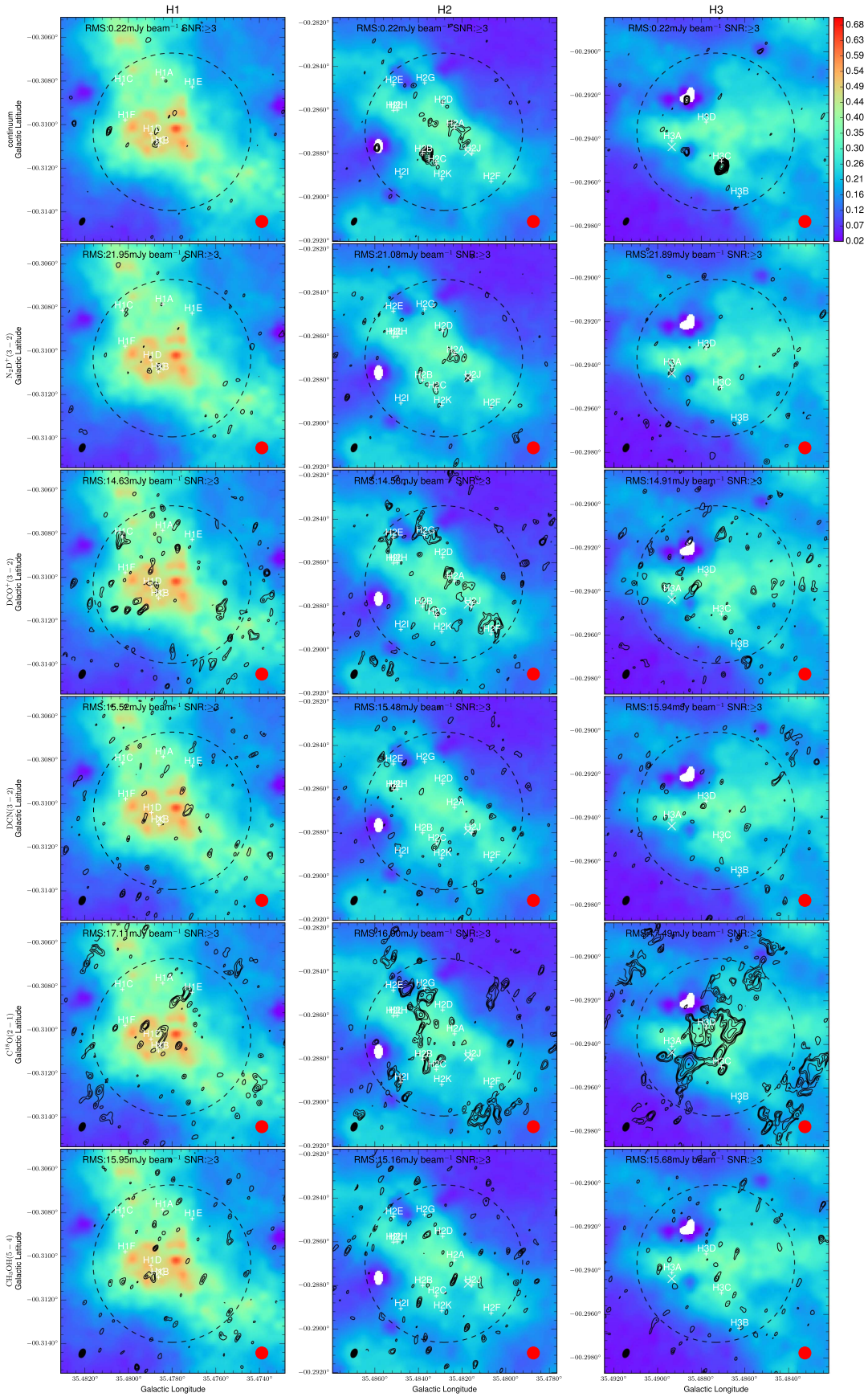

Figure 9. Same as Figure 1, but for sources H1, H2, and H3.

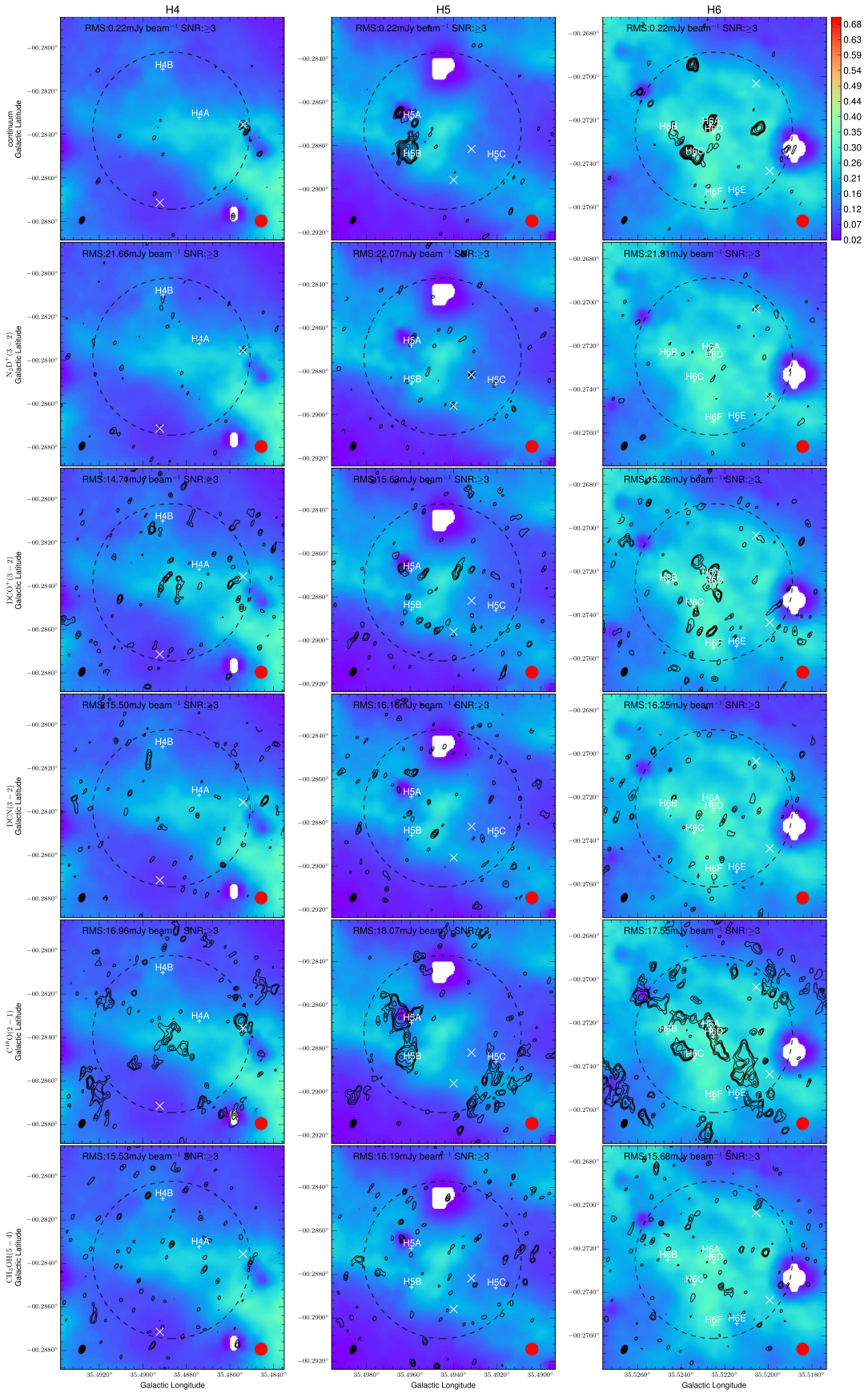

Figure 10. Same as Figure 1, but for sources H4, H5, and H6.

v_{LSR} of each IRDC[9] (see Table 1). We find the strongest detections of N_2D^+(3-2) in the B1, C9, and H2 clumps, which all show extended structures that are also identified as some of the highest N_2D^+(3-2) line flux cores. In general, the strongest cores in a given region (e.g., A1A, A3A, etc) are easily visible in these 0th-moment maps, but many of the weaker cores do not stand out above the noise (lowest contour is $3\sigma \simeq 60$ mJy bm^{-1} km s^{-1}), which is higher than the noise resulting from the more localized velocity ranges used to detect the cores.

In addition, there remain some $\geqslant 4\sigma$ features visible in these region maps that have not been identified as cores (i.e., as connected structures in PPV space). Note, however, that our core search is confined to within the primary beam, so strong features beyond this scale would not have been identified. Because our focus is on the cores, we only note here the position of these "clump-scale" structures (on average, there are about two per region), and discuss below their likelihood of being real features or merely noise fluctuations, by comparison with other tracers.

The third to sixth rows show 0th-moments maps of DCO^+(3-2), DCN(3-2), $C^{18}O$(2-1), and $CH_3OH(v\ \ t=0$ 5(1,4)-4(2,2)), respectively. These images contain a lot of ancillary information, which will not be discussed in detail in this paper. We note that all regions have strong $C^{18}O$(2-1) detection, which tends to trace spatially extended structures (again, subject to the constraints of spatial filtering of the largest scales). The other tracers tend to identify smaller scale structures.

One particular use of these images is to show the presence or absence of these species at the locations of identified N_2D^+(3-2) cores and "clump-scale" structures. Cores will be discussed in more detail in Section 4.2. For the clump-scale structures, several are also seen in these ancillary tracers, e.g., in: DCO^+(3-2), such as the source in A3; DCN(3-2), such as the MIR-bright source in B2; or 1.3 mm continuum, such as sources in C6 (north) and F3 (also seen in CH_3OH). When such coincident detections in independent tracers are seen, it increases our confidence in the reality of the N_2D^+(3-2) detected structure. For the remainder, it is hard to be sure about their reality: more sensitive follow-up observations are needed. There may be several reasons these N_2D^+(3-2) structures are not identified as cores: they may not be well-connected in velocity space; they may not subtend a sufficient angular area compared to the beam; they may be too close to the boundary of the primary beam, where we truncate the core search algorithm; or they may already be attached to an identified core, but have their clump-scale 0th-moment peak slightly displaced from the core peak (e.g., near H2J and H3A).

Physically, some of the N_2D^+(3-2) structures that are only seen in the broader, 5 km s^{-1} velocity range 0th-moment map may represent an early stage of N_2D^+(3-2) core formation, i.e., when the material is less concentrated in position–velocity space. Thus, the follow-up of such structures with higher sensitivity observations is warranted to investigate such a possibility.

[9] The choice of a 5 km s^{-1} integration range makes this analysis consistent with that of T13, which itself was motivated by our previous single dish studies of these IRDCs. The line-width of N_2D^+(3-2) is $\sim$1 km s^{-1}, so a 5 km s^{-1} integration should be enough to include all the cores in these regions, while limiting the amount of extraneous noise. We have carried out tests with 3, 4, 5, and 6 km s^{-1} integrations, and find comparable results. If a 4σ contour shows up in the 5 km s^{-1} integration (fiducial), there are signals at the same position in other maps.

4.2. Identified N_2D^+ Cores

In total, 141 N_2D^+(3-2) cores are found in the 30 data cubes, based on the criteria stated in Section 3. They are labeled as + signs in the second row of Figures 1 through 10. The cores are named based on the ranking of their N_2D^+(3-2) flux within each surveyed region: e.g., A3A is the highest-flux core within the A3 region, followed by A3B, A3C, etc.

Most strong features in the 0th-moment maps are identified, along with many cores that do not show up in these maps. Note, these 0th-moment maps are integrated over a 5 km s^{-1} range. Meanwhile, many weak N_2D^+ cores are typically found in a velocity range much less than 5 km s^{-1} (the narrowest velocity range is 0.30 km s^{-1} by definition, corresponding to two channels, see Section 3). As a result, many of the weak cores do not show up in the region figures, i.e., at the positions of these cores there is no corresponding N_2D^+ contours seen.

We have ranked the cores based on their N_2D^+ 0th-moment flux, and list the strongest 50 of these in Table 2, along with the six cores from T13. The table lists core positions (intensity-weighted center) in Galactic coordinates in columns 2 and 3. Columns 4 and 5 give the velocity range over which the core is detected. Note the N_2D^+(3-2) cube used for core finding has been smoothed to 0.15 km s^{-1} velocity resolution. In general, cores with structures in more channels tend to be more significant. Column 6 shows the intensity-weighted v_{LSR}. and Column 7 shows the N_2D^+(3-2) total line flux, $S_{N_2D^+}$, for each core. Columns 8, 9, and 10 show fluxes at the core position in the continuum image, the DCO^+ (3-2) 0th-moment image, and the $C^{18}O$ (2-1) 0th-moment image (note that the T13 spectral set-up did not have $C^{18}O$ (2-1)). The 0th-moment images of DCO^+ and $C^{18}O$ are integrated within the velocity ranges shown in columns 4 and 5. The relevant signal-to-noise ratio (S/N) is also listed in these columns. Note that sometimes these fluxes can be negative in the case of non-detections where noise or other fluctuations cause the signal to be negative.

Figures 11–13 show the top 15 newly detected N_2D^+(3-2) cores, ordered by N_2D^+(3-2) line flux. Each figure row shows a 10″ by 10″ zoom-in view of the core, centering at the N_2D^+(3-2) intensity weighted center. The first panel in each row shows the 1.3 mm continuum contours, overlaid on the MIREX map (BT12). For all figures, we use the same color scale for the MIREX image.

The second panel shows the N_2D^+ (3-2) integrated intensity (black solid contours) on top of the 1.3 mm continuum emission (same color scale for all sources). The integration for these N_2D^+ (3-2) 0th-moment maps is only over velocity channels in which the core is defined and only including voxels flagged to be in the core. We also show a full 0th-moment integration map as gray dotted contours, which includes all voxels within the velocity ranges. Both types of contour maps start at 2σ and increase with a step of 1σ, with σ being the noise of the full integration map. The gray dotted contours always extend over a wider area than the black ones because the full integration picks up more flux at the core boundary, which is also why the black solid contours are sometimes separated. At the top of the panel, several properties of the core: N_2D^+(3-2) flux, N_2D^+(3-2) 0th-moment map rms, and N_2D^+(3-2) intensity weighted core velocity (sub- and super-scripts are velocity boundaries over which core is detected).

The third, fourth and fifth panels show DCO^+(3-2), $C^{18}O$ (2-1) and SiO(5-4) 0th-moment maps on top of the dust

Table 2
N_2D^+(3-2) Cores

Core	l (deg)	b (deg)	v_{min} (km s^{-1})	v_{max} (km s^{-1})	$\bar{v}$ (km s^{-1})	$S_{N_2D^+}$ (Jy km s^{-1})	$S_{1.30mm}$/S/N (Jy bm^{-1} km s^{-1})	S_{DCO^+}/S/N (Jy bm^{-1} km s^{-1})	$S_{C^{18}O}$/S/N (Jy bm^{-1} km s^{-1})
(1)	(2)	(3)	(4)	(5)	(6)	(7)	(8)	(9)	(10)
1 C9A	28.39894	0.08112	77.05	80.35	78.44	1.4e+00	6.9e−03/30	−8.6e−03/−0.88	−2.3e−01/−21
C1S	28.32194	0.06737	76.90	81.90	79.40	6.3e−01	1.6e−02/59	6.7e−02/8.2	···/···
G2N	34.78101	−0.56816	38.95	43.95	41.45	6.1e−01	1.4e−03/8.3	1.5e−01/14	···/···
2 B1A	19.28744	0.08048	26.40	29.10	27.66	4.6e−01	3.4e−04/1.5	4.4e−02/5.0	2.6e−02/2.7
C1N	28.32508	0.06714	78.68	83.68	81.18	2.7e−01	1.9e−03/6.9	4.6e−02/5.6	···/···
3 H2A	35.48231	−0.28684	44.95	47.20	45.60	2.3e−01	5.4e−04/2.4	4.7e−02/4.7	2.7e−02/2.3
G2S	34.77842	−0.56838	39.30	44.30	41.80	2.2e−01	1.2e−03/6.7	1.1e−01/10	···/···
F1	34.41928	0.24588	53.62	58.62	56.12	1.6e−01	2.9e−03/8.7	1.0e−01/12	···/···
F2	34.43525	0.24140	55.16	60.16	57.66	9.5e−02	3.5e−03/16	1.5e−01/16	···/···
4 B1B	19.28583	0.08304	26.40	27.15	26.76	6.5e−02	7.6e−03/23	3.3e−02/7.0	6.7e−03/1.3
5 C9B	28.39679	0.08314	76.45	77.95	77.30	6.5e−02	1.1e−04/0.32	−1.2e−02/−1.7	−5.4e−02/−7.5
6 H2B	35.48377	−0.28801	45.10	46.90	46.10	6.3e−02	2.6e−03/11	2.5e−02/2.7	4.1e−02/3.9
7 D6A	28.55294	−0.24057	85.50	86.85	86.39	6.0e−02	3.5e−04/0.93	−1.0e−02/−1.2	1.1e−02/1.2
8 D5A	28.56350	−0.23050	87.90	88.95	88.28	5.8e−02	4.3e−04/1.7	2.6e−03/0.33	−2.3e−02/−2.9
9 B2A	19.30983	0.06697	24.90	26.55	25.56	5.6e−02	2.8e−03/9.8	2.8e−02/4.2	5.5e−02/7.5
10 H5A	35.49591	−0.28680	45.10	46.30	45.34	5.2e−02	4.1e−04/1.7	3.3e−02/3.9	2.0e−02/2.2
11 H1A	35.47838	−0.30785	44.20	45.55	44.88	5.0e−02	−2.2e−04/−0.68	2.5e−02/3.0	2.3e−02/2.5
12 H2C	35.48314	−0.28847	44.95	46.45	45.69	4.9e−02	9.0e−04/3.6	2.1e−02/2.6	3.0e−02/3.1
13 F4A	34.45842	0.25645	56.95	58.15	57.40	4.9e−02	1.4e−03/6.4	4.7e−02/6.0	1.5e−02/1.7
14 C3A	28.34951	0.09583	77.35	79.00	78.29	4.9e−02	3.8e−04/1.1	6.7e−03/1.0	−1.7e−02/−2.4
15 C5A	28.35517	0.05754	76.45	77.65	76.80	4.8e−02	−7.0e−05/−0.29	4.0e−03/0.72	1.4e−03/0.22
16 D2A	28.53882	−0.27327	84.45	85.80	84.73	4.8e−02	1.2e−04/0.40	4.0e−04/0.048	−9.0e−03/−0.94
17 H2D	35.48285	−0.28575	44.35	47.20	45.68	4.6e−02	2.8e−04/1.2	2.7e−02/2.4	−5.6e−02/−4.3
18 H2E	35.48511	−0.28485	45.55	46.60	46.08	4.6e−02	1.9e−04/0.51	5.4e−02/7.5	3.5e−04/0.044
19 D2B	28.53645	−0.27670	85.50	86.55	86.11	4.6e−02	1.3e−05/0.047	−1.0e−02/−1.3	−2.5e−03/−0.31
20 C4A	28.35450	0.07184	79.15	80.65	79.87	4.4e−02	5.0e−04/2.2	8.5e−03/1.4	2.3e−02/3.3
21 C2A	28.34592	0.05881	77.35	79.75	78.36	4.3e−02	5.9e−04/1.9	8.1e−03/0.94	−1.6e−02/−1.7
22 C2B	28.34677	0.05918	79.45	79.60	79.50	4.1e−02	2.4e−03/6.5	−3.1e−03/−0.92	−4.9e−03/−1.8
23 A3A	18.80730	−0.30530	64.10	66.05	65.16	3.9e−02	1.8e−03/8.2	2.4e−02/3.3	1.8e−02/2.4
24 D1A	28.52688	−0.25208	87.30	87.90	87.46	3.8e−02	1.3e−04/0.50	1.1e−02/1.8	3.0e−02/4.5
25 A3B	18.80692	−0.30445	63.95	65.90	65.15	3.7e−02	4.3e−05/0.18	1.5e−02/2.1	2.3e−02/3.1
26 H1B	35.47858	−0.31096	43.90	45.40	44.49	3.6e−02	5.5e−04/2.4	9.3e−03/1.1	−8.1e−03/−0.84
27 D2C	28.53883	−0.27762	88.65	88.80	88.75	3.5e−02	1.9e−04/0.57	−3.3e−03/−0.79	4.3e−03/1.0
28 D1B	28.52548	−0.25163	86.40	86.70	86.58	3.5e−02	6.6e−04/2.4	3.3e−03/0.74	1.1e−05/2.1e−3
29 C7A	28.36254	0.12185	79.45	80.50	80.20	3.4e−02	2.8e−04/0.76	−2.5e−03/−0.42	−2.7e−02/−4.6
30 D7A	28.56324	−0.23270	84.45	84.90	84.65	3.3e−02	1.2e−04/0.40	−2.4e−03/−0.46	−1.1e−02/−1.8
31 D2D	28.54054	−0.27463	88.80	89.25	89.09	3.3e−02	−1.0e−04/−0.29	6.1e−04/0.12	−2.6e−03/−0.48
32 D8A	28.57531	−0.23401	84.45	85.50	84.65	3.3e−02	−2.5e−04/−0.78	1.3e−02/1.8	−2.7e−03/−0.32
33 D3A	28.54180	−0.23689	85.80	86.85	86.66	3.3e−02	2.8e−04/1.1	−3.3e−02/−4.5	1.6e−02/2.0
34 C4B	28.35479	0.07069	80.05	80.20	80.14	3.2e−02	9.8e−04/4.4	2.7e−02/8.6	8.2e−03/3.3
35 D9A	28.58601	−0.22902	85.95	87.45	86.63	3.2e−02	−8.4e−05/−0.34	2.1e−03/0.25	−4.8e−04/−0.049
36 D2E	28.53890	−0.27550	87.15	88.65	88.01	3.0e−02	−1.7e−04/−0.71	−5.9e−03/−0.71	−3.1e−02/−3.1
37 B2B	19.30633	0.06616	25.95	27.45	26.74	2.9e−02	1.2e−03/5.2	3.0e−02/4.4	3.1e−02/4.4
38 C9C	28.40155	0.07969	78.70	79.30	78.97	2.8e−02	−8.8e−04/−2.2	4.2e−03/0.92	−5.2e−03/−1.1
39 C4C	28.35621	0.07074	79.15	80.95	79.95	2.8e−02	−2.0e−05/−0.074	5.1e−03/0.72	1.2e−02/1.6
40 H6A	35.52262	−0.27226	44.95	46.15	45.49	2.7e−02	4.8e−03/22	5.0e−02/6.1	1.6e−01/18
41 D1C	28.52562	−0.25044	86.55	86.70	86.64	2.6e−02	3.0e−05/0.12	1.1e−03/0.36	−5.4e−03/−1.2
42 C2C	28.34311	0.06017	78.40	80.20	79.14	2.6e−02	8.8e−03/39	2.9e−02/3.8	1.3e−01/15
43 H2F	35.48063	−0.28927	45.10	46.60	46.02	2.5e−02	5.2e−04/1.4	−5.6e−04/−0.068	−2.4e−02/−2.5
44 H3A	35.48931	−0.29409	42.40	44.65	43.33	2.5e−02	2.9e−04/1.1	4.0e−02/3.9	−3.4e−03/−0.28
45 D7B	28.56577	−0.23133	89.10	89.25	89.24	2.5e−02	−1.4e−04/−0.62	2.7e−03/0.65	−7.8e−03/−2.3
46 C6A	28.36492	0.05084	80.20	81.25	80.63	2.4e−02	−3.2e−04/−1.1	1.2e−02/2.3	8.0e−03/1.4
47 H2G	35.48368	−0.28475	45.10	45.25	45.25	2.4e−02	3.2e−05/0.11	1.7e−02/5.9	6.4e−03/1.5
48 D3B	28.54043	−0.23394	87.60	88.65	87.83	2.4e−02	4.6e−04/1.9	1.5e−02/2.0	3.8e−02/4.7
49 D8B	28.57318	−0.23559	88.50	89.25	88.72	2.3e−02	1.2e−04/0.35	−2.4e−03/−0.36	−8.2e−03/−1.2
50 D2F	28.53729	−0.27641	87.30	87.45	87.40	2.3e−02	7.2e−04/3.0	−2.8e−03/−0.67	−4.0e−03/−1.2

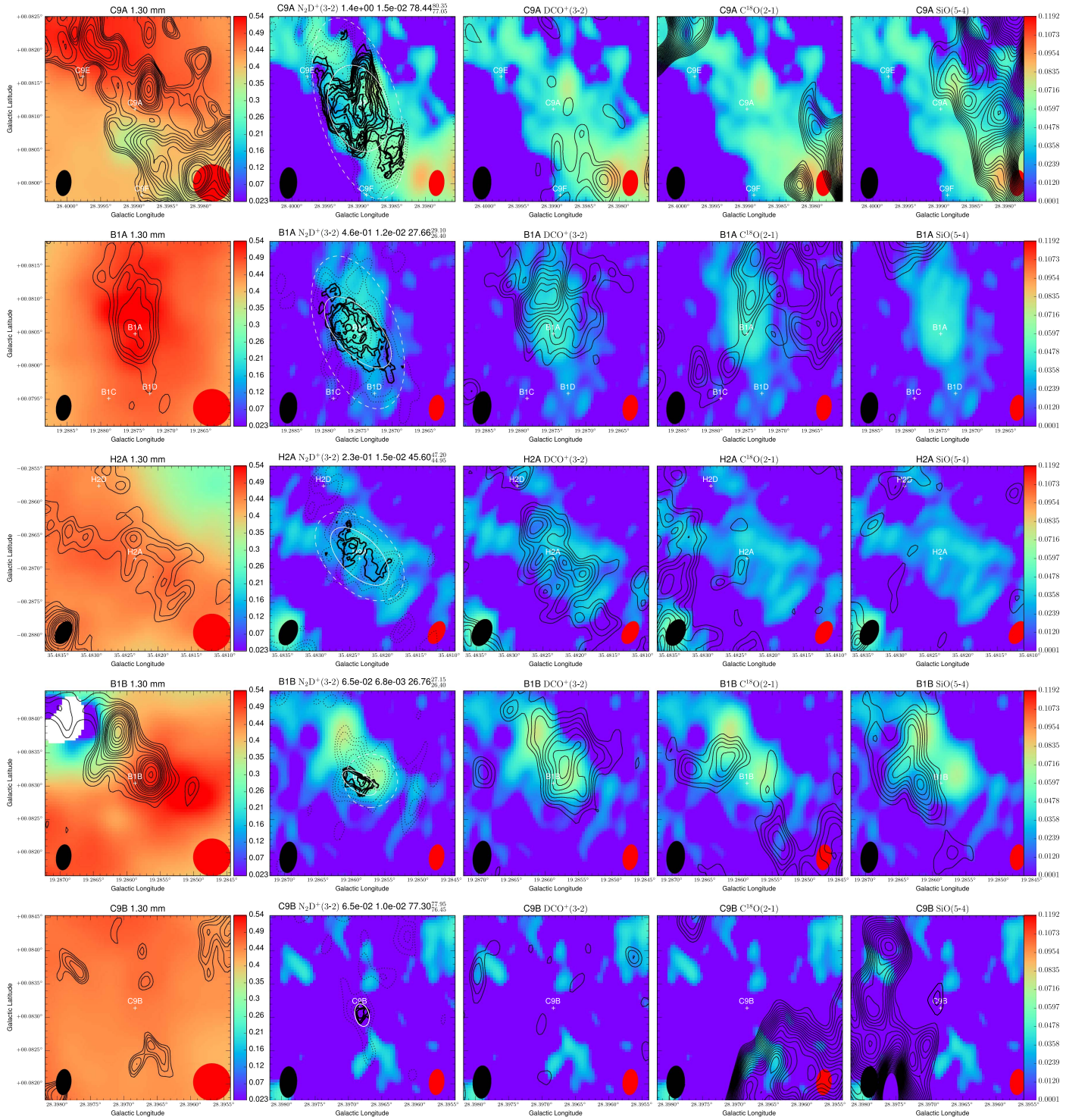

Figure 11. Core-scale zoom-in figures of C9A, B1A, H2A, B1B, C9B (rows top to bottom, also following rank order of $N_2D^+(3-2)$ flux). Each panel shows a 10″ by 10″ FOV. The first column shows 1.3 mm continuum (contours: 2, 3, 4, 5, 7, 9, 11, 13, 15, 17, 20, 40, 60, 80... σ, where $1\sigma \simeq 2.2 \times 10^{-4}$ Jy bm^{-1}; *ALMA* beam in lower left) overlaid on MIREX (BT12) mass surface density (color scale in g cm^{-2}; *Spitzer* beam in lower right). 2nd column shows 0th-moment $N_2D^+(3-2)$ of the cores (only including core voxels), shown as the solid contours: 2, 3, 4, 5...σ (beam lower left), overlaid on the 1.30 mm continuum (beam lower right). The dotted contours are the full integration of the cores (including all voxels within the channels). At the top of the panel we list total $N_2D^+(3-2)$ flux (in Jy bm^{-1} km s^{-1}), $N_2D^+(3-2)$ 0th-moment map rms (in Jy bm^{-1} km s^{-1}), and $N_2D^+(3-2)$ intensity weighted core velocity and velocity range (in km s^{-1}). The solid and dashed ellipses are fitted boundaries to the cores (see text). 3rd column is the same as the 2nd, except contours now show $DCO^+(3-2)$ integrated over the same velocity range as the N_2D^+ core. 4th column is the same as the 2nd, except contours now show $C^{18}O(2-1)$ integrated over the same velocity range as the N_2D^+ core. 5th column is the same as the 2nd, except contours now show SiO(5-4) integrated over the 5 km s^{-1} velocity range used in the region maps.

continuum. For $DCO^+(3-2)$ and $C^{18}O$ (2-1), the integrations are over the same velocity ranges as the $N_2D^+(3-2)$ 0th-moment map. For SiO(5-4) the velocity range is the 5 km s^{-1} range used in the region maps (note a full analysis of the SiO(5-4) data from the region maps will be presented in a companion paper by M. Liu et al. 2016, in preparation).

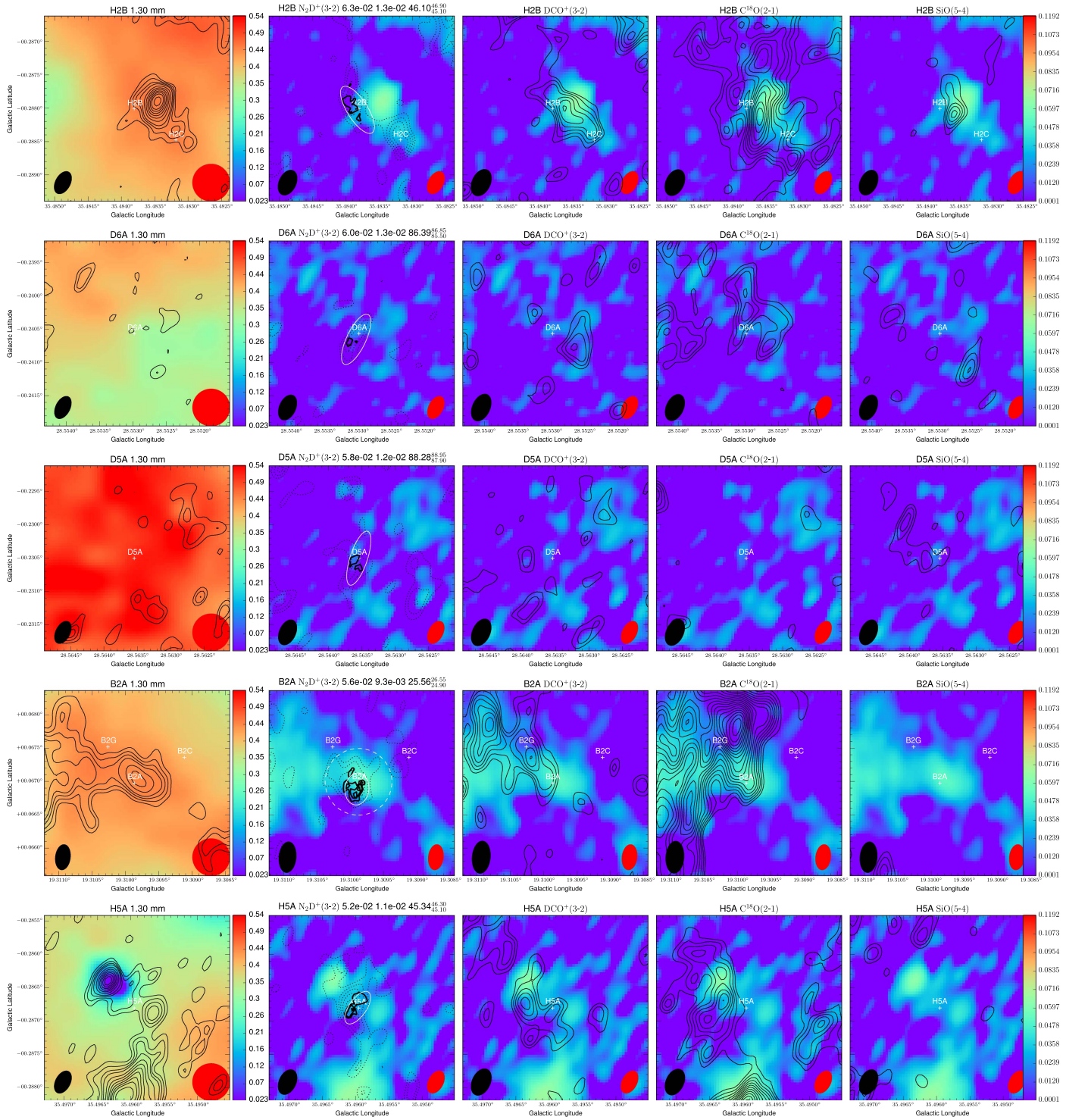

Figure 12. Same as Figure 11, but for H2B, D6A, D5A, B2A, H5A.

Comparing some of the top ranked cores, including those of T13 (see Table 2), C9A has more than twice the N_2D^+(3-2) flux of C1-S. B1A ranks above C1-N, and H2A ranks above F1. Note that the integration for C9A, B1B, H2A only includes voxels in the connected components (the defined cores), so their fluxes are higher in a full integration (i.e., gray dotted contours in these core figures). However, we also note that the sensitivity in this data set is about 3 times worse than T13, so the uncertainty in core fluxes is also higher.

One of the features of the 6 N_2D^+(3-2) cores found by T13 was their extended DCO^+(3-2) envelopes. This is still true for most of the new cores presented here, however, now we also see some cores, like C9A, C9B, D5A, C3A and C5A, which have relatively weak DCO^+(3-2) emission. This chemical diversity may reflect different environmental conditions among the core sample.

We note that there is often a dearth of $C^{18}O$(2-1) emission associated with the N_2D^+(3-2) cores, which likely indicates that

there is a high degree of gas phase depletion of CO, i.e., due to freeze out onto dust grain ice mantles. Such CO depletion is thought to boost the deuteration of N_2H^+ (e.g., K15), and so this anti-correlation of CO emission with N_2D^+ emission is expected theoretically.

SiO(5-4) emission is a known tracer of protostellar outflows and so can help us assess such activity within the cores. C9A and C9B show extended SiO emission in their vicinity, which is however thought to mostly arise from a separate massive protostellar source (e.g., that is seen as a strong DCN(3-2) source in the lower right of the region Figure 5) (M. Liu et al. 2016, in preparation). However, there is some localized, potentially elongated SiO emission that is spatially coincident with C9A, which likely indicates that this core is already forming a protostar (similar to that present in C1-S Feng et al. 2016; Tan et al. 2016). Most other cores do not show strong SiO(5-4) emission. We discuss more details about the six strongest N_2D^+(3-2) cores below.

In order to study basic core properties and, for the best cases of C9A, B1A, H2A, B1B, B2A and F4A, compare to simple dynamical models, we fit 2D elliptical Gaussians to the N_2D^+(3-2) integrated intensity maps. We define an ellipse at the 3σ value of the 2D Gaussian (Case 1), which is shown as the white, solid ellipses in the N_2D^+(3-2) columns of Figures 11 to 13. These fitting results are listed in Table 3 for the best six cores. Note that the 2D Gaussian center is sometimes slightly different from the intensity weighted core center defined earlier (Table 2). Note also that the N_2D^+(3-2) 0th-moment image, e.g., for C9A, has an rms of 13 mJy per $1\farcs5 \times 1\farcs0$ beam km s^{-1}, roughly corresponding to 23 mJy per $2\farcs3 \times 2\farcs0$ km s^{-1}, which is about twice the rms of C1 region rms reported by T13. Thus the core sizes reported here are likely to be systematically somewhat smaller than if they had been measured with the same sensitivity used by T13. Still, we will use these ellipses for our following study of core dynamics. For C9A, B1A, H2A, B1B, B2A and F4A we also consider their properties on the scale of larger ellipses (Case 2), shown by the dashed ellipses in Figures 11–13). These geometries are based on total N_2D^+(3-2) intensities: they cover most of the N_2D^+ flux within the 2σ contours from the full integration images. These ellipses also cover most of the 1.3 mm continuum flux that is seen to be associated with these cores. These core properties are shown inside square brackets in Table 3. We note that given these uncertainties in defining core sizes, we have not attempted to derive deconvolved sizes. As discussed above, our Case 1 radii are probably lower limits, and deconvolution would have only a very minor effect on the derived Case 2 radii.

In the following sections, we study the core dynamics, following the methods of T13. We focus on 6 cores C9A, B1A, H2A, B1B, B2A, and F4A. The first four of these are the top four in terms of N_2D^+(3-2) flux of the new cores presented in this paper (see Table 2). They all have clear associations with 1.3 mm continuum structures, which will be the preferred method of estimated masses. B2A and F4A have relatively weak N_2D^+(3-2) fluxes, but also show quite good correspondence with continuum sources.

4.3. Core Kinematics

Only the top four ranked N_2D^+(3-2) cores are significantly larger than the beam. For these, Figure 14 shows the first-moment maps of this species, along with DCO^+(3-2) and $C^{18}O$(3-2). Only voxels with $\geqslant 3\sigma$ detection are considered. C9A shows a strong velocity gradient in N_2D^+(3-2): in the upper left part of the image, the mean velocities are $\simeq -1.5$km s^{-1}, whereas they are $\simeq +0.5$ km s^{-1} on the lower right. The core diameter is about 0.1 pc, so the velocity gradient is $\sim$20 km s^{-1} pc^{-1}. Given the bimodal morphology of the 0th-moment map, it is possible that we are seeing two N_2D^+(3-2) cores in the process of merging. The other cores, B1A and H2A, do not show such large velocity gradients.

Figure 15 shows the second-moment (velocity dispersion) maps of C9A, B1A and H2A in N_2D^+(3-2), DCO^+(3-2) and $C^{18}O$(3-2). Again, only voxels with $\geqslant 3\sigma$ detection are considered. A 0.242 km s^{-1} effective dispersion from the N_2D^+(3-2) main hyperfine group is subtracted in quadrature from its maps. Regions that then have a negative result are shown as blank; here, the sensitivity is probably too low to obtain a good measure of the velocity dispersion. Note also this effect leads to the appearance of artificially low dispersion halos around the main features. The C9A N_2D^+(3-2) second-moment map shows a higher velocity dispersion on its left-hand side than its right. Again, this may be evidence in favor of the two merging cores scenario.

Within the defined Case 1 ellipses of C9A, B1A, H2A, B1B, B2A, and F4A, we extract total flux density from each channel (full velocity resolution of 0.04 km s^{-1}) and convert it to main beam temperature, $T_{\rm mb}$, to derive the total spectrum as a function of $v_{\rm LSR}$. These are shown in Figure 16. We then fit the N_2D^+(3-2) line with full blended hyperfine components, utilizing the HFS method of the CLASS software package,[10] assuming the line is optically thin (this was shown to be good approximation in the cores studied by T13). The resulting centroid velocity $V_{\rm LSR,N_2D^+}$ and 1D velocity dispersion $\sigma_{\rm N_2D^+,obs}$ are listed in Table 3. The velocity dispersions derived by this method range from about 0.2 to 0.6 km s^{-1}. However, to estimate the total velocity dispersion that is needed for the dynamical analysis, we subtract the N_2D^+ thermal component from its velocity dispersion in quadrature (assuming 10 K temperature), and add back the core sound speed in quadrature, assuming a mean particle mass $\mu = 2.33 m_p$ and gas temperature of 10 ± 3 K, following T13. These results, listed as $\sigma_{\rm N_2D^+}$ in Table 3, are slightly larger, ranging from 0.26 to 0.61 km s^{-1}.

4.4. Core Masses

Following the methods of T13, we measure core masses, M_c, within the Case 1 and Case 2 ellipses in two ways. First, we use the MIREX map of BT12. As a first MIREX-based estimate, we use the total mass surface density in the map integrated over the area of the core to yield a mass, $M_{c,\rm max}$. As a second MIREX-based estimate, we account for the clump mass surface density, $\Sigma_{\rm cl}$, in an elliptical annulus around the core (from R_c to $2R_c$ in the case of a circular core), and then subtract this contribution to Σ within the core ellipse, to then yield a mass, $M_{c,\rm min}$.

As discussed by T13, depending on the 3D structure of the core and clump, there can be large differences between $M_{c,\rm max}$ and $M_{c,\rm min}$. In some favorable situations where $\Sigma_{\rm cl}$ is relatively small, both methods will yield similar mass estimates. However, there can be cases where the surrounding "clump" has a higher inferred mass surface density, and so $M_{c,\rm min}$ is formally negative; i.e., this mass estimate is not well-defined.

[10] http://www.iram.fr/IRAMFR/GILDAS

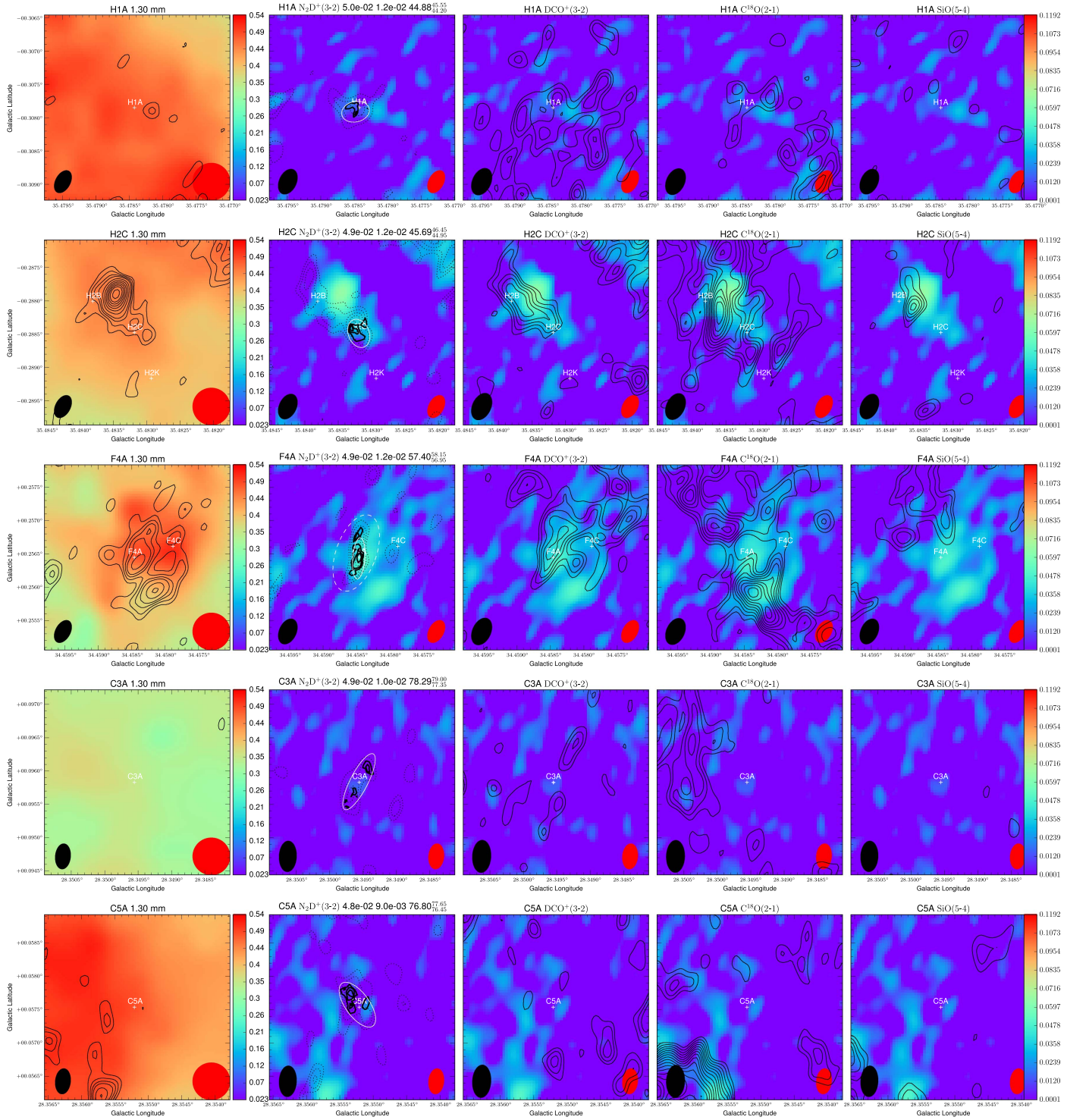

Figure 13. Same as Figure 11, but for H1A, H2C, F4A, C3A, C5A.

In fact, this situation arises for C9A, because the N_2D^+(3-2) core is not co-located with a MIREX Σ peak. Another problem with the MIREX-based mass estimates is that the maps can suffer "saturation" in high Σ regions, i.e., where $\Sigma \gtrsim 0.5$ g cm^{-2} (see BT12). This leads to the MIREX-based mass estimate being an underestimate of the true core mass.

As a second method, we calculate core masses from their 1.3 mm continuum emission, $M_{c,\mathrm{mm}}$. We use Equation (7) from T13. For consistency, we also assume a dust temperature of $T_d = 10 \pm 3$ K (such cold temperatures are expected for highly deuterated cores; see also discussion of T13) and adopt $\kappa_\nu = 5.95 \times 10^{-3}$ cm^2 g^{-1} (Ossenkopf & Henning 1994). We adopt a 30% uncertainty for κ_ν. We do not attempt to carry out clump envelope subtraction with this method, because the ALMA observations tend to filter out the larger scale emission from the clump. Because the uncertainties in temperature cause

Table 3
Physical Properties of the Six "Best" N_2D^+ Cores

Core property (% error)	C9A	B1A	H2A	B1B	B2A	F4A	Average
l (°)	28.39896	19.28747	35.48231	19.28584	19.30986	34.45843	...
	[28.39896]	[19.28747]	[35.48231]	[19.28567]	[19.30983]	[34.45846]	...
b (°)	0.08113	0.08050	−0.28681	0.08305	0.06689	0.25643	...
	[0.08113]	[0.08050]	[−0.28681]	[0.08308]	[0.06699]	[0.25651]	...
θ_c (″)	1.94	1.65	1.42	0.707	0.745	0.606	...
	[3.30]	[3.05]	[2.28]	[1.44]	[1.80]	[1.53]	...
e	0.747	0.877	0.852	0.881	0.672	0.955	...
	[0.904]	[0.866]	[0.781]	[0.00]	[0.00]	[0.866]	...
P.A. (°)	16	42	45	58	83	85	...
	[16]	[20]	[45]	[0]	[0]	[70]	...
d (kpc) (20%)	5.0	2.4	2.9	2.4	2.4	3.7	...
R_c (0.01 pc) (20%)	4.71	1.92	2.00	0.822	0.867	1.09	...
	[7.99]	[3.55]	[3.20]	[1.67]	[2.09]	[2.74]	...
V_{LSR,N_2D^+} (km s^{-1})	78.40 ± 0.02	27.60 ± 0.02	45.50 ± 0.02	26.60 ± 0.04	25.50 ± 0.03	57.10 ± 0.05	...
	[78.40 ± 0.03]	[27.50 ± 0.02]	[45.50 ± 0.03]	[26.70 ± 0.04]	[25.50 ± 0.04]	[57.10 ± 0.11]	...
$\sigma_{N_2D^+,obs}$ (km s^{-1})	0.579 ± 0.028	0.351 ± 0.025	0.245 ± 0.029	0.296 ± 0.068	0.180 ± 0.029	0.329 ± 0.053	...
	[0.579 ± 0.028]	[0.351 ± 0.025]	[0.245 ± 0.029]	[0.296 ± 0.068]	[0.180 ± 0.029]	[0.329 ± 0.053]	...
$\sigma_{N_2D^+,nt}$ (km s^{-1})	0.576 ± 0.028	0.347 ± 0.025	0.239 ± 0.030	0.291 ± 0.069	0.172 ± 0.030	0.325 ± 0.053	...
	[0.576 ± 0.028]	[0.347 ± 0.025]	[0.239 ± 0.030]	[0.291 ± 0.069]	[0.172 ± 0.030]	[0.325 ± 0.053]	...
$\sigma_{N_2D^+}$ (km s^{-1})	0.606 ± 0.028	0.395 ± 0.026	0.304 ± 0.029	0.347 ± 0.062	0.255 ± 0.029	0.375 ± 0.049	...
	[0.606 ± 0.028]	[0.395 ± 0.026]	[0.304 ± 0.029]	[0.347 ± 0.062]	[0.255 ± 0.029]	[0.375 ± 0.049]	...
Σ_{cl} (g cm^{-2}) (30%)	0.317	0.394	0.321	0.361	0.293	0.313	...
	[0.312]	[0.321]	[0.292]	[0.362]	[0.273]	[0.288]	...
$\Sigma_{c,max}$ (g cm^{-2}) (30%)	0.282	0.492	0.327	0.391	0.302	0.349	...
	[0.308]	[0.438]	[0.326]	[0.437]	[0.297]	[0.334]	...
$M_{c,max}$ ($M_\odot$) (50%)	9.34	2.70	1.95	0.394	0.338	0.616	...
	[29.3]	[8.24]	[4.99]	[1.83]	[1.94]	[3.74]	...
$n_{H,c,max}$ (10^5 cm^{-3}) (36%)	6.17	26.5	16.9	49.1	35.9	33.1	...
	[3.97]	[12.7]	[10.5]	[26.9]	[14.6]	[12.6]	...
$\sigma_{c,vir,max}$ (km s^{-1})	0.514 ± 0.064	0.398 ± 0.050	0.348 ± 0.044	0.241 ± 0.030	0.220 ± 0.027	0.259 ± 0.032	...
	[0.681 ± 0.086]	[0.500 ± 0.063]	[0.430 ± 0.054]	[0.353 ± 0.044]	[0.334 ± 0.042]	[0.399 ± 0.050]	...
$\sigma_{N_2D^+}/\sigma_{c,vir,max}$	1.18 ± 0.14	0.992 ± 0.129	0.873 ± 0.130	1.44 ± 0.30	1.16 ± 0.18	1.45 ± 0.25	1.18 ± 0.08
	[0.890 ± 0.108]	[0.790 ± 0.103]	[0.707 ± 0.105]	[0.982 ± 0.208]	[0.763 ± 0.123]	[0.941 ± 0.163]	[0.845 ± 0.057]
$R_{c,vir,max}$ (0.01 pc)	4.02 ± 1.03	1.94 ± 0.49	1.83 ± 0.46	0.774 ± 0.198	0.796 ± 0.204	1.04 ± 0.26	...
	[7.18 ± 1.84]	[3.75 ± 0.96]	[3.06 ± 0.78]	[1.66 ± 0.42]	[1.98 ± 0.50]	[2.67 ± 0.68]	...
$R_c/R_{c,vir,max}$	1.17 ± 0.33	0.989 ± 0.282	1.09 ± 0.31	1.06 ± 0.30	1.09 ± 0.31	1.05 ± 0.29	1.07 ± 0.12
	[1.11 ± 0.31]	[0.946 ± 0.270]	[1.05 ± 0.29]	[1.01 ± 0.28]	[1.06 ± 0.30]	[1.03 ± 0.29]	[1.03 ± 0.12]
$\Sigma_{c,min}$ (g cm^{-2}) (30%)	-	0.0979	6.37e−3	0.0303	8.68e−3	0.0368	...
	-	[0.117]	[0.0342]	[0.0743]	[0.0243]	[0.0457]	...
$M_{c,min}$ ($M_\odot$) (50%)	-	0.537	0.0380	0.0305	9.72e−3	0.0650	...
	-	[2.20]	[0.522]	[0.311]	[0.159]	[0.511]	...
$n_{H,c,min}$ (10^5 cm^{-3}) (36%)	-	5.26	0.329	3.80	1.03	3.49	...
	-	[3.39]	[1.10]	[4.58]	[1.20]	[1.72]	...
$\sigma_{c,vir,min}$ (km s^{-1})	-	0.266 ± 0.033	0.130 ± 0.016	0.127 ± 0.016	0.0905 ± 0.0114	0.148 ± 0.018	...
	-	[0.359 ± 0.045]	[0.245 ± 0.030]	[0.227 ± 0.028]	[0.179 ± 0.022]	[0.243 ± 0.030]	...
$\sigma_{N_2D^+}/\sigma_{c,vir,min}$	-	1.49 ± 0.19	2.34 ± 0.34	2.74 ± 0.57	2.82 ± 0.45	2.54 ± 0.43	2.38 ± 0.18
	-	[1.10 ± 0.14]	[1.24 ± 0.18]	[1.53 ± 0.32]	[1.43 ± 0.23]	[1.55 ± 0.26]	[1.37 ± 0.10]
$R_{c,vir,min}$ (0.01 pc)	-	0.865 ± 0.222	0.255 ± 0.065	0.215 ± 0.055	0.135 ± 0.034	0.338 ± 0.086	...
	-	[1.94 ± 0.49]	[0.991 ± 0.254]	[0.687 ± 0.176]	[0.565 ± 0.145]	[0.987 ± 0.253]	...

Table 3
(Continued)

Core property (% error)	C9A	B1A	H2A	B1B	B2A	F4A	Average
$R_c/R_{c,vir,min}$	-	2.22 ± 0.63	7.84 ± 2.24	3.82 ± 1.09	6.42 ± 1.83	3.22 ± 0.92	4.70 ± 0.65
	-	$[1.83 \pm 0.52]$	$[3.23 \pm 0.92]$	$[2.44 \pm 0.69]$	$[3.71 \pm 1.06]$	$[2.78 \pm 0.79]$	$[2.80 \pm 0.36]$
$S_{1.30mm}$ (mJy)	31.3 ± 0.8	9.63 ± 0.69	5.52 ± 0.61	10.3 ± 0.3	4.36 ± 0.31	1.96 ± 0.26	...
	$[76.4 \pm 1.3]$	$[20.1 \pm 1.2]$	$[10.7 \pm 0.9]$	$[27.6 \pm 0.6]$	$[14.2 \pm 0.7]$	$[7.24 \pm 0.66]$	...
$S_{1.30mm}/\Omega$ (MJy/sr)	112 ± 2	47.6 ± 3.4	37.1 ± 4.1	274 ± 7	107 ± 7	71.9 ± 9.6	...
	$[95.0 \pm 1.7]$	$[29.1 \pm 1.8]$	$[28.2 \pm 2.5]$	$[183 \pm 3]$	$[59.3 \pm 3.1]$	$[41.5 \pm 3.8]$	...
$\Sigma_{c,mm}$ (g cm^{-2})	$2.10^{4.21}_{1.24}$	$0.895^{1.79}_{0.530}$	$0.698^{1.40}_{0.413}$	$5.15^{10.3}_{3.05}$	$2.01^{4.03}_{1.19}$	$1.35^{2.71}_{0.800}$	...
	$[1.79^{3.58}_{1.06}]$	$[0.547^{1.10}_{0.324}]$	$[0.531^{1.06}_{0.314}]$	$[3.44^{6.89}_{2.03}]$	$[1.12^{2.23}_{0.660}]$	$[0.781^{1.56}_{0.462}]$	...
$M_{c,mm}$ ($M_\odot$)	$69.7^{146}_{31.7}$	$4.91^{10.3}_{2.24}$	$4.16^{8.71}_{1.90}$	$5.19^{10.9}_{2.36}$	$2.26^{4.73}_{1.03}$	$2.39^{5.00}_{1.09}$	...
	$[170^{357}_{77.6}]$	$[10.3^{21.6}_{4.69}]$	$[8.11^{17.0}_{3.70}]$	$[14.4^{30.1}_{6.55}]$	$[7.29^{15.3}_{3.32}]$	$[8.73^{18.3}_{3.98}]$	...
$n_{H,c,mm}$ (10^5 cm^{-3})	$45.9^{93.8}_{25.5}$	$48.0^{98.1}_{26.6}$	$35.9^{73.4}_{19.9}$	644^{1320}_{357}	239^{489}_{133}	$128^{261}_{71.0}$	...
	$[23.0^{47.0}_{12.8}]$	$[15.8^{32.4}_{8.79}]$	$[17.1^{34.9}_{9.47}]$	$[211^{432}_{117}]$	$[54.8^{112}_{30.4}]$	$[29.3^{59.9}_{16.3}]$	...
$\sigma_{c,vir,mm}$ (km s^{-1})	$0.849^{1.03}_{0.681}$	$0.462^{0.561}_{0.371}$	$0.421^{0.511}_{0.338}$	$0.458^{0.556}_{0.368}$	$0.353^{0.429}_{0.283}$	$0.364^{0.442}_{0.292}$	...
	$[1.06^{1.28}_{0.849}]$	$[0.528^{0.641}_{0.424}]$	$[0.486^{0.590}_{0.390}]$	$[0.592^{0.718}_{0.475}]$	$[0.465^{0.565}_{0.373}]$	$[0.493^{0.599}_{0.396}]$	...
$\sigma_{N_2D^+}/\sigma_{c,vir,mm}$	$0.714^{0.890}_{0.588}$	$0.854^{1.06}_{0.703}$	$0.723^{0.901}_{0.595}$	$0.758^{0.944}_{0.624}$	$0.722^{0.900}_{0.594}$	$1.03^{1.29}_{0.850}$	$0.800^{0.882}_{0.742}$
	$[0.573^{0.715}_{0.472}]$	$[0.747^{0.931}_{0.615}]$	$[0.626^{0.781}_{0.516}]$	$[0.586^{0.731}_{0.483}]$	$[0.548^{0.683}_{0.451}]$	$[0.761^{0.948}_{0.627}]$	$[0.640^{0.705}_{0.594}]$
$R_{c,vir,mm}$ (0.01 pc)	$11.0^{16.1}_{6.82}$	$2.62^{3.83}_{1.62}$	$2.67^{3.91}_{1.66}$	$2.81^{4.11}_{1.74}$	$2.06^{3.01}_{1.28}$	$2.05^{3.00}_{1.27}$	...
	$[17.3^{25.3}_{10.7}]$	$[4.20^{6.14}_{2.61}]$	$[3.90^{5.72}_{2.42}]$	$[4.67^{6.83}_{2.90}]$	$[3.83^{5.61}_{2.38}]$	$[4.08^{5.97}_{2.53}]$	...
$R_c/R_{c,vir,mm}$	$0.429^{0.657}_{0.288}$	$0.733^{1.12}_{0.493}$	$0.749^{1.15}_{0.504}$	$0.293^{0.448}_{0.197}$	$0.421^{0.646}_{0.283}$	$0.531^{0.814}_{0.357}$	$0.526^{0.646}_{0.452}$
	$[0.462^{0.708}_{0.310}]$	$[0.846^{1.30}_{0.569}]$	$[0.820^{1.26}_{0.551}]$	$[0.359^{0.550}_{0.241}]$	$[0.547^{0.838}_{0.367}]$	$[0.672^{1.03}_{0.451}]$	$[0.617^{0.757}_{0.531}]$

quite asymmetric uncertainties in $\Sigma_{c,mm}$ and $M_{c,mm}$, we calculate lower and upper boundaries and put them in sub- and super- scripts in Table 3. Overall, including temperature, opacity, and distance uncertainties, the total uncertainty is about a factor of two in the mass estimation (see detailed discussion in T13); however, because of the difficulties of clump envelope subtraction in the MIREX mass estimates, we prefer the mm continuum-based mass estimate as our fiducial method. We note that, for a "core" contained within the synthesized beam size, at a distance of 5 kpc and with a dust temperature of 10 K, the 1σ mass sensitivity is 0.51 $M_\odot$.

With these methods, we find that C9A is the most massive of the six cores suitable for dynamical analysis, with $M_{c,mm} \simeq 70\ M_\odot$ in the Case 1 (i.e., inner) ellipse. The other cores are at least ten times smaller in mass. Considering the Case 2 (i.e., larger) ellipses, C9A rises in mass to $M_{c,mm} \simeq 170\ M_\odot$. On these scales, the other cores have about 10 $M_\odot$.

4.5. Core Dynamics

Following T13 and MT03, we consider virialized singular polytropic quasi-spherical cores that have surfaces in approximate pressure equilibrium with their surrounding clump environments. Such cores have a radius $R_{c,vir}$ and internal velocity dispersion $\sigma_{c,vir}$ (assuming some contribution from large scale B-fields such that the Alfvén Mach number in the core is unity). The two quantities are calculated following T13 Equations (2) and (4), given core mass M_c and clump mass surface density Σ_{cl}. For each core, we calculate the properties in three cases: (1) using the core mass derived from the MIREX map without envelope subtraction; (2) using the core mass from the MIREX map with envelope subtraction; (3) using the core mass derived from the 1.3 mm continuum map. The clump mass surface density is estimated from the MIREX map in the region from R_c to $2R_c$ (in the case of a circular core). Table 3 lists the results for the six considered cores.

For our preferred mass estimates via 1.3 mm continuum emission, we find a mean ratio of the observed to predicted virial velocity dispersion for the six cores of $\langle \sigma_{N_2D^+}/\sigma_{c,vir,mm} \rangle = 0.80$. This is very similar to the result found by T13 of a ratio of 0.83 for the six cores they analyzed. It suggests that this core population (of 12 cores) has properties that are consistent with the virial equilibrium assumption of the MT03 Turbulent Core model.

The most massive core, C9A, has a ratio of 0.71, which is modestly subvirial. As discussed by T13, apparently subvirial cores may indicate that stronger large scale magnetic fields are present: the fiducial MT03 model assumes that large-scale B-fields are present, which would produce an Alfvén Mach number of unity for turbulence in the core. T13 argued that stronger B-fields, $\sim$1 mG, were needed in the massive cores of their sample, especially C1-S, if the cores were to be in virial equilibrium. We carry out a similar analysis here, to work out what B-field strengths are needed for virial equilibrium, summarizing the results in Table 4. The magnetic field strengths that are implied by the fiducial MT03 model are again $\sim$1 mG. They need to be raised modestly to achieve precise virial equilibrium. Also listed is the B-field strength, $B_{c,crit}$, needed to make the core mass equal to the magnetic critical mass (Bertoldi & McKee 1992): these also tend to be slightly higher.

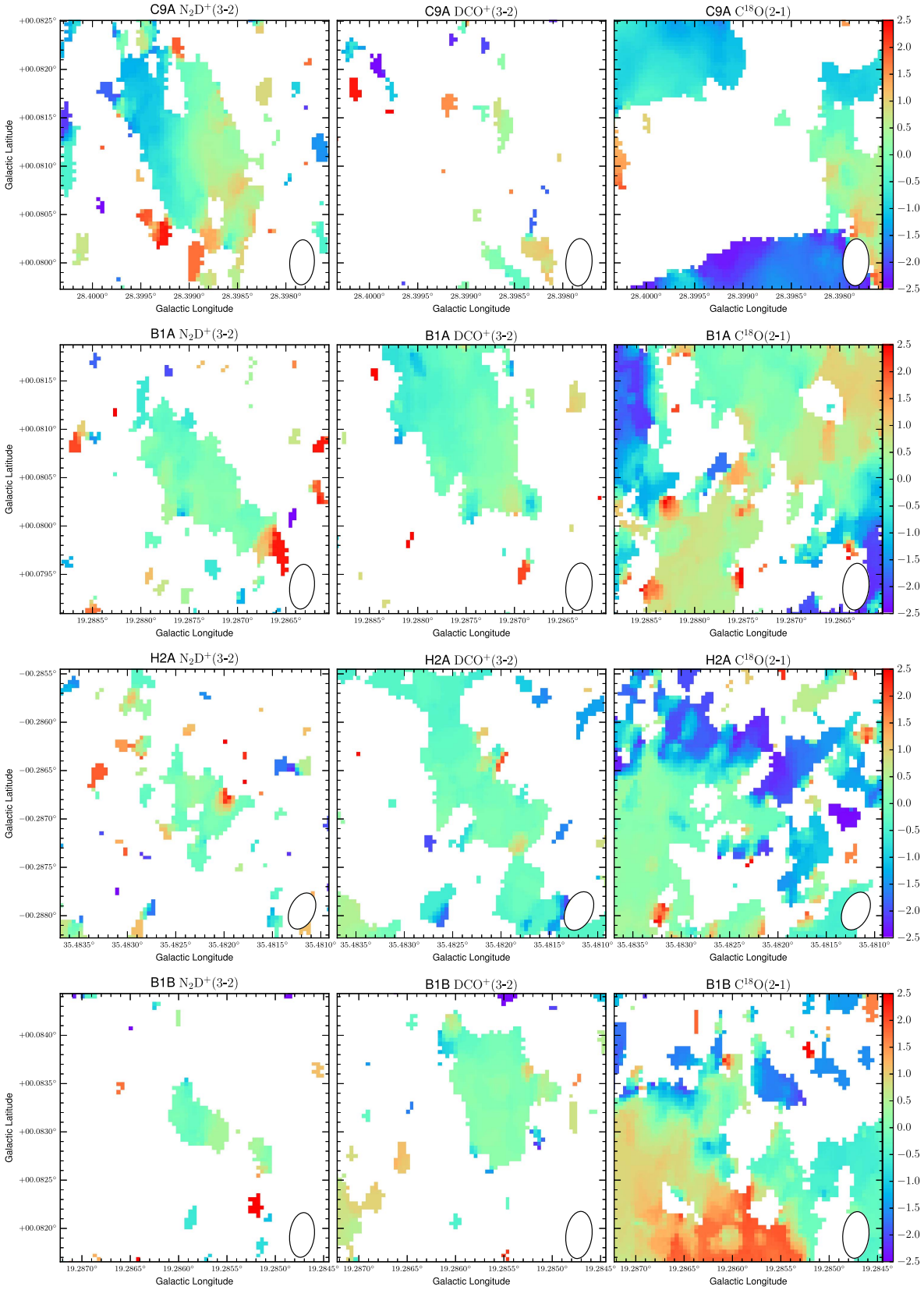

Figure 14. First-moment (intensity-weighted v_{LSR}) maps of the top four ranked N_2D^+(3-2) cores C9A (first row), B1A (second row), H2A (third row), B1B (fourth row), in N_2D^+ (first column), DCO^+ (second column), $C^{18}O$ (third column). The calculation is within a 5 km s^{-1} range centered on N_2D^+(3-2) v_{LSR} (Table 2). Only voxels with $\geqslant 3\sigma$ intensity are considered and shown in color. The color scale is linear from -2.5 to $+2.5$ km s^{-1}. The synthesized beam is shown in the lower-right corner.

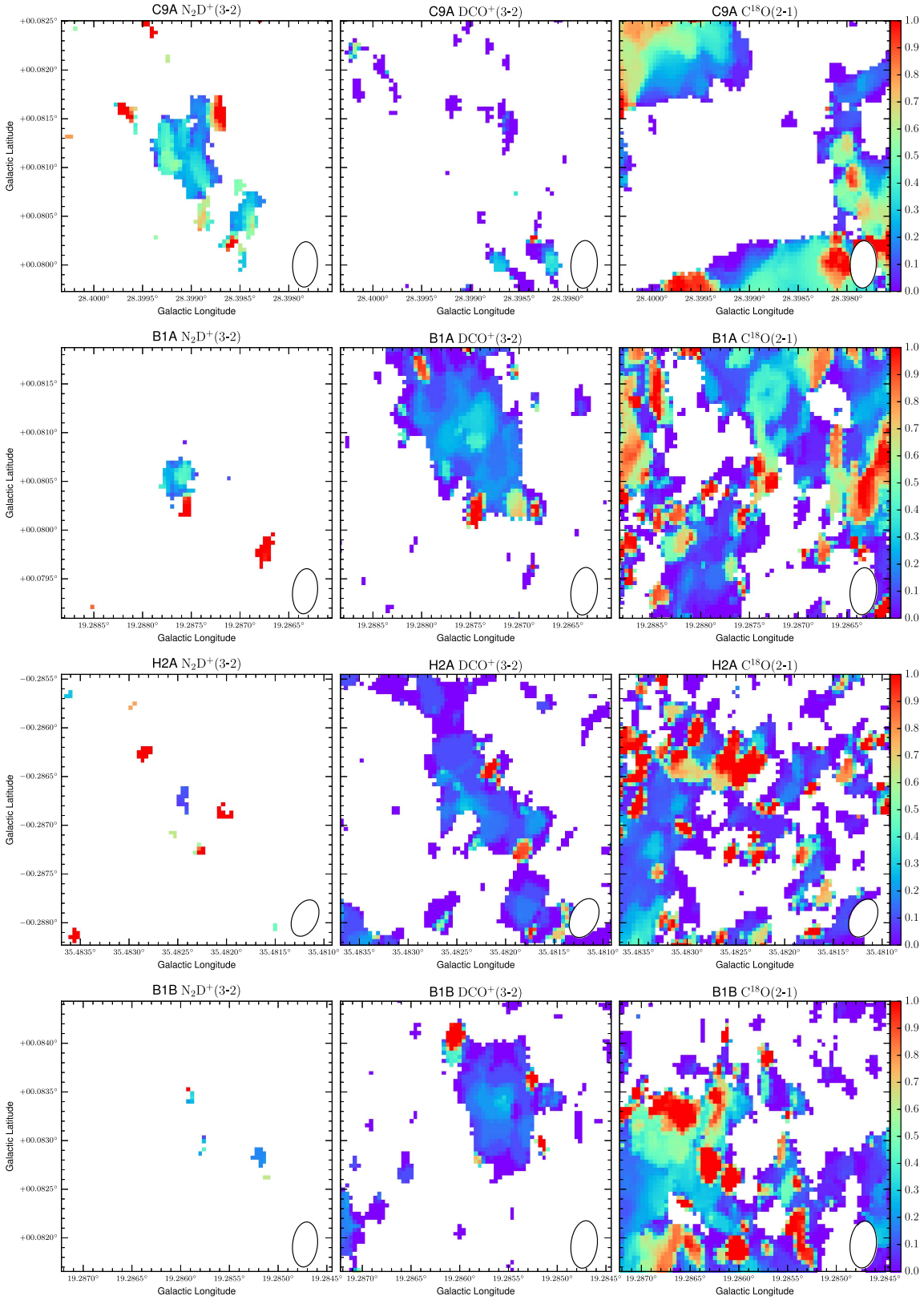

Figure 15. Second-moment (intensity-weighted velocity dispersion) maps of the top four ranked N_2D^+(3-2) cores C9A (first row), B1A (second row), H2A (third row), B1B (fourth row), in N_2D^+ (first column), DCO^+ (second column), $C^{18}O$ (third column). The calculation is within a 5 km s^{-1} range, centered on N_2D^+ v_{LSR} (Table 2). Only voxels with $\geqslant 3\sigma$ intensity are considered and shown in color. For the N_2D^+ data, a 0.242 km s^{-1} contribution to the dispersion from the main group of hyperfine structures is subtracted in quadrature. However, we see in some regions the second-moment pixels shrink from the first-moment images. This is mainly due to the fact that the velocity span is narrower than 0.242 km s^{-1}. In these areas, we are limited by the sensitivity. The color scale is linear from 0 to 1.0 km s^{-1}. The synthesized beam is shown in the lower-right corner.

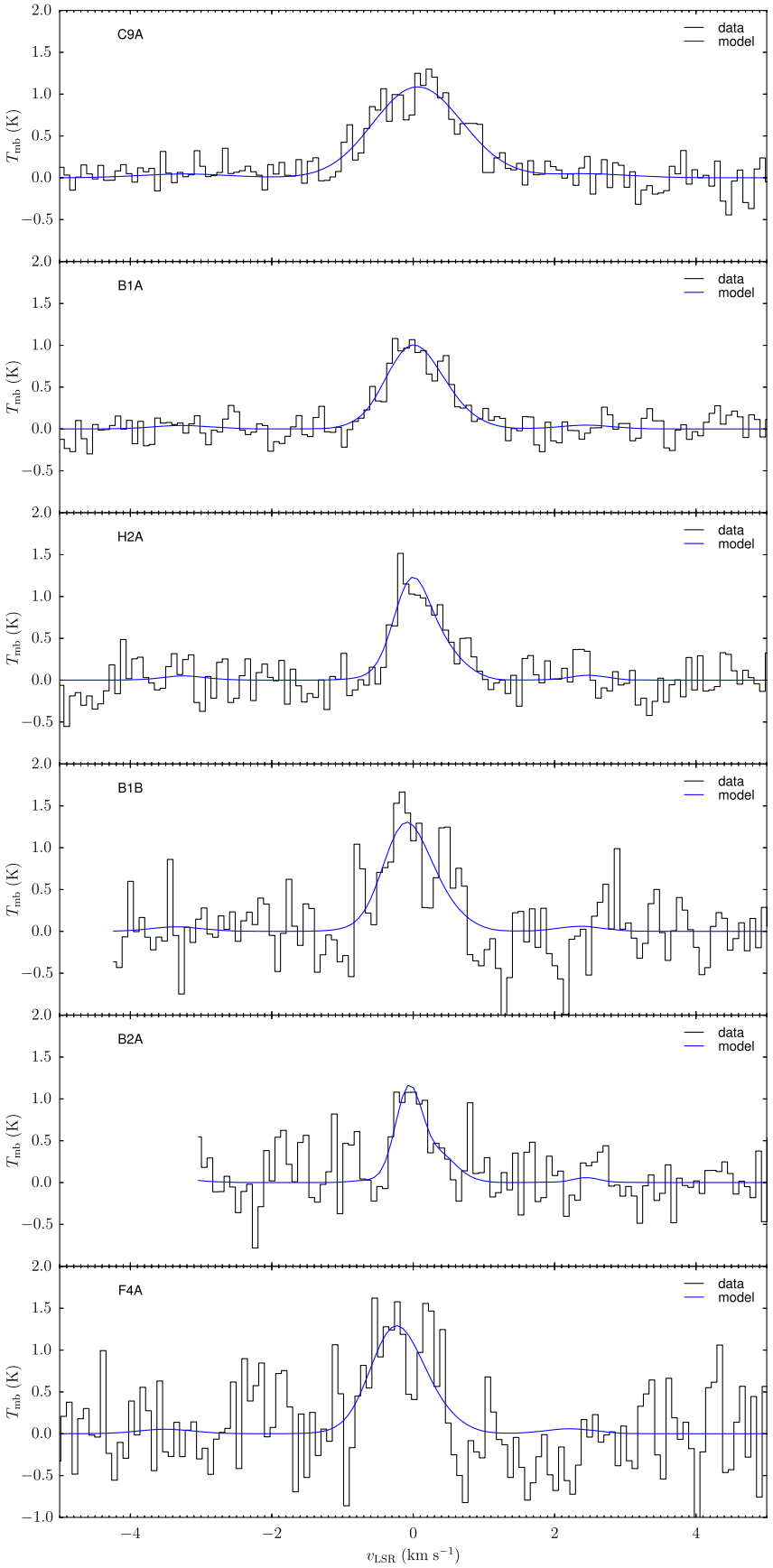

Figure 16. N_2D^+(3-2) core spectra (black) and their HFS fit results (blue). All spectra are in the rest frame of their centroid velocity $V_{\rm LSR,N_2D^+}$, derived from the HFS fit. The core names are labeled on the top left. Note that the spectra shown are binned to have 0.08 km s^{-1} spectral resolution, whereas the HFS fit results are drawn from their maximum velocity resolution of 0.04 km s^{-1}.

Table 4
Dynamical Properties of the Six "Best" N_2D^+ Cores

Core property (% error)	C9A	B1A	H2A	B1B	B2A	F4A
R_c (0.01 pc) (20%)	4.71	1.92	2.00	0.822	0.867	1.09
$\sigma_{N_2D^+}$ (km s^{-1})	0.606 ± 0.028	0.395 ± 0.026	0.304 ± 0.029	0.347 ± 0.062	0.255 ± 0.029	0.375 ± 0.049
Σ_{cl} (g cm^{-2}) (30%)	0.317	0.394	0.321	0.361	0.293	0.313
$M_{c,mm}$ ($M_\odot$)	$69.7^{146}_{31.7}$	$4.91^{10.3}_{2.24}$	$4.16^{8.71}_{1.90}$	$5.19^{10.9}_{2.36}$	$2.26^{4.73}_{1.03}$	$2.39^{5.00}_{1.09}$
$\alpha_c \equiv 5\sigma^2_{N_2D^+}R_c/(GM_{c,mm})$[a]	$0.287^{0.636}_{0.124}$	$0.702^{1.56}_{0.299}$	$0.514^{1.14}_{0.211}$	$0.220^{0.501}_{0.0775}$	$0.288^{0.644}_{0.115}$	$0.742^{1.66}_{0.288}$
$n_{H,c,mm}$ (10^5 cm^{-3})	$45.9^{93.8}_{25.5}$	$48.0^{98.1}_{26.6}$	$35.9^{73.4}_{19.9}$	644^{1320}_{357}	239^{489}_{133}	$128^{261}_{71.0}$
$t_{c,ff}$ (10^5 yr)[b]	$0.204^{0.273}_{0.142}$	$0.199^{0.267}_{0.139}$	$0.230^{0.309}_{0.161}$	$0.0544^{0.0730}_{0.0380}$	$0.0892^{0.120}_{0.0624}$	$0.122^{0.164}_{0.0853}$
B_c (μG) ($m_A = 1$)	1220^{1750}_{903}	812^{1160}_{598}	541^{780}_{393}	2620^{3830}_{1800}	1170^{1690}_{842}	1260^{1830}_{899}
$R_{c,vir,mm}$ (0.01 pc)	$11.0^{7.17}_{16.3}$	$2.62^{1.71}_{3.89}$	$2.67^{1.74}_{3.97}$	$2.81^{1.83}_{4.18}$	$2.06^{1.34}_{3.06}$	$2.05^{1.34}_{3.05}$
$R_c/R_{c,vir,mm}$	$0.429^{0.657}_{0.288}$	$0.733^{1.12}_{0.493}$	$0.749^{1.15}_{0.504}$	$0.293^{0.448}_{0.197}$	$0.421^{0.646}_{0.283}$	$0.531^{0.814}_{0.357}$
$\sigma_{c,vir,mm}$ (km s^{-1})	$0.849^{1.03}_{0.681}$	$0.462^{0.561}_{0.371}$	$0.421^{0.511}_{0.338}$	$0.458^{0.556}_{0.368}$	$0.353^{0.429}_{0.283}$	$0.364^{0.442}_{0.292}$
$\sigma_{N_2D^+}/\sigma_{c,vir,mm}$	$0.714^{0.890}_{0.588}$	$0.854^{1.06}_{0.703}$	$0.723^{0.901}_{0.595}$	$0.758^{0.944}_{0.624}$	$0.722^{0.900}_{0.594}$	$1.03^{1.29}_{0.850}$
$\phi_{B,vir}$	$6.87^{11.5}_{3.82}$	$4.27^{7.16}_{2.37}$	$6.65^{11.2}_{3.70}$	$5.87^{9.85}_{3.26}$	$6.68^{11.2}_{3.71}$	$2.58^{4.32}_{1.43}$
$m_{A,vir}$	$0.519^{0.772}_{0.383}$	$0.711^{1.18}_{0.506}$	$0.529^{0.791}_{0.390}$	$0.573^{0.874}_{0.419}$	$0.528^{0.788}_{0.389}$	$1.08^{3.36}_{0.704}$
$B_{c,vir}$ (μG)	2350^{3670}_{1360}	1140^{1830}_{582}	1020^{1620}_{564}	4570^{7230}_{2500}	2220^{3530}_{1200}	1160^{1980}_{307}
$B_{c,crit}$ (μG)	2830^{4730}_{1700}	1200^{2010}_{725}	939^{1570}_{565}	6930^{11600}_{4170}	2710^{4530}_{1630}	1820^{3040}_{1090}

Notes.
[a] Virial parameter (Bertoldi & McKee 1992).
[b] Core free-fall time, $t_{c,ff} = [3\pi/(32G\rho_c)]^{1/2} = 1.38^5(n_{H,c,mm}/10^5\ \mathrm{cm}^{-3})^{-1/2}$ yr.

4.6. Notes on Individual Cores

4.6.1. C9A

C9A shows the strongest and most extended N_2D^+ structure (Figure 5). As discussed above, it shows complex kinematics, potentially indicative of two merging structures, which have now become connected in their N_2D^+ emission. C9A appears to be in a very active, chaotic region (see Figures 5 and 11). We see strong detections of 1.3 mm continuum, especially a large filamentary structure that contains C9A. The mm emission also shows evidence for potential fragmentation or localized heating within the C9A structure. We also see strong detections of DCO^+, DCN, $C^{18}O$, and CH_3OH from other sources in the vicinity, but not overlapping with C9A. This core is close to an H II region IRAS18402-0403, in the direction toward the lower right of the figure (mostly out of the FOV), following the mm continuum filament. Battersby et al. (2010) have studied this area (GLM4 clump) with continuum and molecular line data (not including N_2D^+). Zhang et al. (2009) studied this area (their P2 clump) and found two 1.3 mm continuum cores and an NH_3 core. They correspond to the continuum sources to the south of C9A (about 7″ away, see Figures 5 and 11). We checked the Herschel 70 μm image in this area. There are two sources. The larger source corresponds to the H II region. Next to it is a smaller source, about half that size, which corresponds to the continuum source to the lower-right (Figure 11). C9A is at the boundary of the smaller source.

As discussed above, there is extended, strong SiO(5-4) emission in the surroundings of C9A, likely driven from the strong continuum sources to the lower left. However, C9A also has a weak, small SiO(5-4) counterpart. This only shows up on the red side of the spectrum. The small SiO counterpart is detected from ~82 to 89 km s^{-1}, whereas C9A is detected from 77.05 to 80.35 km s^{-1}. No SiO emission on the blue side is detected (the lower limit of velocity is ~22.5 km s^{-1}). We also check that there is no overlap between the N_2D^+ core and the SiO connected structures in the PPV space, again using the graph method. It is unclear whether the small SiO(5-4) counterpart in the C9A N_2D^+ core is part of the outflow from the external strong continuum source, or whether it indicates the presence of an already-formed protostar within the core (similar to that present in C1-S Feng et al. 2016; Tan et al. 2016). This question will be investigated further by M. Liu et al. (2016, in preparation).

4.6.2. B1A

B1A appears to be in a more quiescent, isolated environment. It shows an elongated morphology, and has relatively weak 1.3 mm continuum counterpart (compared to C9A). We have detected SiO(5-4) emission to the north of B1A outside the continuum boundary. This does not appear to be originating from a protostellar source within the B1A core. However, due to the limited spectral coverage in the blue wing side, we cannot see if there is a symmetric SiO structure on the other side of the B1A core.

Schlingman et al. (2011) have studied this region as one of the BGPS sources (Aguirre et al. 2011 with 33" spatial resolution). They observed HCO^+(3-2) and N_2H^+(3-2) lines with 30″ resolution. Their study is on the clump scale. At this scale, they found a velocity dispersion of about 1.5 km s^{-1}, which is about a factor of five larger than our measurement at core scale with N_2D^+(3-2). We checked the Herschel 70 μm image in this area. B1A has no 70 μm counterpart, and is in a 70 μm dark area.

4.6.3. H2A

H2A appears to be in a quiescent environment. It has no detectable SiO(5-4) emission and a relatively weak 1.3 mm continuum counterpart (compared to C9A). H2A's continuum shows an "X-shaped" structure. We checked the Herschel 70 μm image in this area, finding that H2A has no corresponding 70 μmm source.

4.6.4. B1B

B1B is about 10″ away from B1A (Figure 2). It is displaced in velocity from B1A by about 1 km s^{-1}. It has a strong 1.3 mm continuum counterpart (Figure 11). There is a MIR-bright source (visible as a "hole" in the MIREX map) nearby.

4.6.5. B2A

B2A corresponds to a continuum core that is at the end of a group of 1.3 mm continuum sources that also contains a MIR-bright source.

4.6.6. F4A

F4A corresponds to one of a pair of spatially adjacent 1.3 mm continuum sources. The other source does not show significant N_2D^+emission. Overall, this is a relatively quiescent environment.

5. DISCUSSION AND CONCLUSIONS

We have carried out a survey of 32 IRDC clumps, designed to detect cores with strong N_2D^+(3-2) emission. Such cores may be massive analogs of low-mass pre-stellar or early-stage protostellar cores. This work stems from the pilot study of T13, which identified six such cores in four IRDC clumps. Our current survey has a lower line sensitivity level than T13, but a similar 1.3 mm continuum sensitivity. The spectral set-up includes several ancillary line tracers, such as DCO^+(3-2), DCN(3-2), $C^{18}O$(2-1) and SiO(5-4). We have also utilized the MIREX maps of these regions developed by Butler et al. (2014) and BT12.

In order to process the larger number of target regions, we have presented a new way to automatically identify N_2D^+(3-2) cores as connected structures in PPV space using Graph theory methods.

In total, 141 N_2D^+(3-2) core candidates were identified via these automated methods, although many of the weakest sources are likely to be noise fluctuations. The locations of these sources are identified in our maps of the clump-scale regions. We have presented properties of the strongest 50 cores, including their mean velocities and velocity ranges, as well as their N_2D^+(3-2) line fluxes. We have presented zoom-in maps of the top 15 of these cores, and a dynamical analysis of the best six among these sources.

The main results are: the identification of the very massive (up to $\sim$170 $M_\odot$) C9A N_2D^+(3-2) "core," i.e., a connected structure in ppv space, which shows complex structure and kinematics. Several other $\sim$10 $M_\odot$ cores are found. The N_2D^+(3-2) velocity dispersions are consistent with the predictions of the turbulent core model of MT03, based on quasi virial equilibrium of such structures. Further follow-up work is needed to test for the starless nature of these cores, especially examining outflow tracers.

The methods presented in this study should also be applied to larger samples of clumps to identify their N_2D^+(3-2) core populations, which may be key for understanding the origin of the stellar initial mass function and the formation of star clusters.

We thank Brian Svoboda for helpful comments and suggestions. JCT and SK acknowledge an NRAO/SOS grant and NSF grant AST1411527. PC acknowledges the financial support of the European Research Council (ERC; project PALs 320620). This paper makes use of the following ALMA data: ADS/JAO.ALMA#2013.1.00806.S. ALMA is a partnership of ESO (representing its member states), NSF (USA) and NINS (Japan), together with NRC (Canada), NSC and ASIAA (Taiwan), and KASI (Republic of Korea), in cooperation with the Republic of Chile. The Joint ALMA Observatory is operated by ESO, AUI/NRAO, and NAOJ. The National Radio Astronomy Observatory is a facility of the National Science Foundation operated under cooperative agreement by Associated Universities, Inc.

Facility: ALMA.

REFERENCES

Aguirre, J. E., Ginsburg, A. G., Dunham, M. K., et al. 2011, ApJS, 192, 4
Battersby, C., Bally, J., Jackson, J. M., et al. 2010, ApJ, 721, 222
Bergin, E. A., & Tafalla, M. 2007, ARA&A, 45, 339
Bertoldi, F., & McKee, C. F. 1992, ApJ, 395, 140
Bonnell, I. A., Bate, M. R., Clarke, C. J., & Pringle, J. E. 2001, MNRAS, 323, 785
Butler, M. J., & Tan, J. C. 2009, ApJ, 696, 484
Butler, M. J., & Tan, J. C. 2012, ApJ, 754, 5
Butler, M. J., Tan, J. C., & Kainulainen, J. 2014, ApJL, 782, L30
Carey, S. J., Noriega-Crespo, A., Mizuno, D. R., et al. 2009, PASP, 121, 76
Caselli, P., & Ceccarelli, C. 2012, A&ARv, 20, 56
Crapsi, A., Caselli, P., Walmsley, C. M., et al. 2005, ApJ, 619, 379
Feng, S., Beuther, H., Zhang, Q., et al. 2016, ApJ, 828, 100
Hagberg, A. A., Schult, D. A., & Swart, P. J. 2008, in Proc. 7th Python in Science Conf. (SciPy2008), ed. G. Varoquaux, T. Vaught, & J. Millman (Pasadena, CA: SciPy Conference), 11
Henshaw, J. D., Jimenez-Serra, I., Longmore, S. N., et al. 2016, arXiv:1608.00009
Hernandez, A. K., & Tan, J. C. 2015, ApJ, 809, 154
Kong, S., Caselli, P., Tan, J. C., Wakelam, V., & Sipilä, O. 2015, ApJ, 804, 98
Kong, S., Tan, J. C., Caselli, P., et al. 2016, ApJ, 821, 94
McKee, C. F., & Tan, J. C. 2003, ApJ, 585, 850
McLaughlin, D. E., & Pudritz, R. E. 1997, ApJ, 476, 750
Ossenkopf, V., & Henning, T. 1994, A&A, 291, 943
Rathborne, J. M., Jackson, J. M., & Simon, R. 2006, ApJ, 641, 389
Schlingman, W. M., Shirley, Y. L., Schenk, D. E., et al. 2011, ApJS, 195, 14
Smith, B. D., Turk, M. J., Sigurdsson, S., O'Shea, B. W., & Norman, M. L. 2009, ApJ, 691, 441
Svoboda, B. E., Shirley, Y. L., Battersby, C., et al. 2016, ApJ, 822, 59
Tackenberg, J., Beuther, H., Henning, T., et al. 2012, A&A, 540, A113
Tan, J. C., Kong, S., Butler, M. J., Caselli, P., & Fontani, F. 2013, ApJ, 779, 96
Tan, J. C., Kong, S., Zhang, Y., et al. 2016, ApJL, 821, L3
Traficante, A., Fuller, G. A., Peretto, N., Pineda, J. E., & Molinari, S. 2015, MNRAS, 451, 3089
Wang, P., Li, Z.-Y., Abel, T., & Nakamura, F. 2010, ApJ, 709, 27
Zhang, Q., Wang, K., Lu, X., & Jiménez-Serra, I. 2015, ApJ, 804, 141
Zhang, Q., Wang, Y., Pillai, T., & Rathborne, J. 2009, ApJ, 696, 268
Zhang, Y., Tan, J. C., & Hosokawa, T. 2014, ApJ, 788, 166